January 2014

Improving Satellite Quantitative Precipitation Estimates By Incorporating Deep Convective Cloud Optical Depth

Ronald Stenz

IMPROVING SATELLITE QUANTITATIVE PRECIPITATION ESTIMATES BY
INCORPORATING DEEP CONVECTIVE CLOUD OPTICAL DEPTH

by

Ronald D. Stenz
Bachelor of Science, Cornell University, 2012

A Thesis
Submitted to the Graduate Faculty

of the

University of North Dakota

In partial fulfillment of the requirements

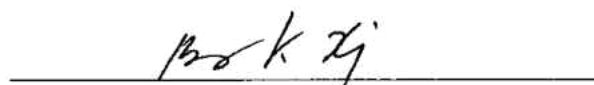for the degree of

Master of Science

Grand Forks, North Dakota
August
2014

This thesis, submitted by Ronald Stenz in partial fulfillment of the requirements for the Degree of Master of Science from the University of North Dakota, has been read by the Faculty Advisory Committee under whom the work has been done and is hereby approved.

_____
Chairperson

_____

_____

This thesis meets the standards for appearance, conforms to the style and format requirements of the Graduate School of the University of North Dakota, and is hereby approved.

_____
Dean of the Graduate School

_____
Date

July 15, 2014

iii

PERMISSION

Title   Improving Satellite Quantitative Precipitation Estimates By Incorporating Deep Convective Cloud Optical Depth

Department   Atmospheric Science

Degree   Master of Science

      In presenting this thesis in partial fulfillment of the requirements for a graduate degree from the University of North Dakota, I agree that the library of the University shall make it freely available for inspection. I further agree that permission for extensive copying for scholarly purposes may be granted by the professor why supervised my thesis work or, in his absence, by the chairperson of the department of the dean of the Graduate School. It is understood that any copying or publication or other use of the thesis or part thereof for financial gain shall not be allowed without my written permission. It is also understood that due recognition shall be given to me and to the University of North Dakota in any scholarly use which may be made of any material in my thesis.

Ronald Stenz_____

_7/15/2014_____

TABLE OF CONTENTS

LIST OF FIGURES

Figure   Page

LIST OF TABLES

x

ACKNOWLEDGEMENTS

I would like to thank my advisor, Dr. Xiquan Dong for his guidance and support, and for providing me the opportunity to work on this research. Additionally, I would like to thank the remainder of my advisement committee, Dr. Baike Xi and Dr. Matthew Gilmore for their comments, suggestions, and expert input into this thesis.

I would also like to thank Dr. Mark Askelson for his guidance and advice on objective analyses performed in this research. My grateful thanks are also extended to the members of my research group, as well as the remaining faculty, staff, and graduate students of the Department of Atmospheric Sciences at the University of North Dakota. Lastly, I want to thank my parents for their support during my life and academic pursuits.

ABSTRACT

As Deep Convective Systems (DCSs) are responsible for most severe weather events, increased understanding of these systems along with more accurate satellite precipitation estimates will improve NWS (National Weather Service) warnings and monitoring of hazardous weather conditions. A DCS can be classified into convective core (CC) regions (heavy rain), stratiform (SR) regions (moderate-light rain), and anvil (AC) regions (no rain). These regions share similar infrared (IR) brightness temperatures (BT), which can create large errors for many existing rain detection algorithms. This study assesses the performance of the National Mosaic and Multi-sensor Quantitative Precipitation Estimation System (NMQ) Q2, and a simplified version of the GOES-R Rainfall Rate algorithm (also known as the Self-Calibrating Multivariate Precipitation Retrieval, or SCaMPR), over the state of Oklahoma (OK) using OK MESONET observations as ground truth. While the average annual Q2 precipitation estimates were about 35% higher than MESONET observations , there were very strong correlations between these two data sets for multiple temporal and spatial scales. Additionally, the Q2 estimated precipitation distributions over the CC, SR, and AC regions of DCSs strongly resembled the MESONET observed ones, indicating that Q2 can accurately capture the precipitation characteristics of DCSs although it has a wet bias. SCaMPR retrievals were typically three to four times higher than the collocated MESONET observations, with relatively weak correlations during a year of comparisons in 2012.

Overestimates from SCaMPR retrievals that produced a high false alarm rate were primarily caused by precipitation retrievals from the anvil regions of DCSs when collocated MESONET stations recorded no precipitation. A modified SCaMPR retrieval algorithm, employing both cloud optical depth and IR temperature, has the potential to make significant improvements to reduce the SCaMPR false alarm rate of retrieved precipitation especially over non-precipitating (anvil) regions of a DCS. Preliminary testing of this new algorithm to identify precipitating area has produced significant improvements over the current SCaMPR algorithm. This modified version of SCaMPR can be used to provide precipitation estimates in gaps of radar and rain gauge coverage to aid in hydrological and flood forecasting.

CHAPTER I

INTRODUCTION

Deep Convective Systems

As a large portion of rainfall and the majority of severe weather reports in the United States arise from Deep Convective Systems (DCSs), improved understanding and satellite Quantitative Precipitation Estimates (QPEs) of these systems are important. DCSs are common in the United States, particularly in the Great Plains, Midwest, and Southeast during spring and summer, with the majority of rainfall occurring at night. DCSs are characterized by a thick mixed phase cloud region capable of producing intense precipitation, strong winds, and hail, and thinner ice clouds often encircling the thick mixed phase cloud region. DCSs typically form in warm and humid conditions, and are capable of growing to hundreds of miles in diameter and persisting for a day or more in extreme cases. DCSs can be separated into convective core (CC), stratiform (SR), and anvil cloud (AC) regions with the most intense precipitation in CC regions, light to moderate precipitation in the SR regions, and light or no precipitation in AC regions (Feng et al. 2011 and 2012).

Figure 1. Visual representation of the hybrid classification system from Feng et al. 2011. Region (1) represents the CC region, (2) represents the SR region, (3) and (4) comprise the AC region, and (5) is a component of a category referred to as Error/Thin Anvil later in this manuscript.

This three-category classification is a simplified version of the classifications shown in Figure 1 from Feng et al. 2011. The CC region can be identified by radar, and is characterized by high reflectivity values using the convective-stratiform algorithm originally developed in Steiner et al. (1995) and modified by Feng et al. (2011). The SR region identified by radar accounts for precipitation echoes that fall below the convective dBZ threshold (Steiner et al. 1995). AC regions can partially be identified by radar, typically by using an echo height threshold, but limited power returns from anvil regions frequently make these clouds undetectable by ground-based precipitation radars such as the WSR-88D. However, the advantage to GOES satellites is that they can detect the entire

cloud shield, including regions of the anvil, typically thin anvil, which is undetectable by radar. Combining GOES and radar data allows the tracking and examination of entire DCSs and their life cycles.

Overview of Satellite QPEs

In addition to rain gauge networks, sources for Quantitative Precipitation Estimates (QPEs) such as satellites and ground-based radars are critical to the National Oceanic and Atmospheric Administration (NOAA)/National Weather Service (NWS) flood and river forecasts (Zhang and Qi 2010; Zhang et al. 2011). Each instrument has both strengths and limitations. Rain gauges provide direct measurements of rainfall, but provide the coarsest spatial and temporal resolution. Radars can provide precipitation estimates with much finer spatial and temporal resolution than rain gauge networks, but suffer from larger sources of errors than rain gauges face. Geostationary satellite QPEs provide continuous coverage, but have larger uncertainties and sources of error than rain gauge observations or radar based estimates. Previous studies document the limitations rain gauge networks face in spatial coverage and the problems radar estimates have with overshooting, the radar beam traveling over the top of precipitation and not detecting it, and beam blockage, along with limited spatial coverage (Krajewski and Smith 2002; Scofield and Kuligowski 2003; Smith et al. 1996; Zhang and Qi 2010; Zhang et al. 2011). QPEs derived from geostationary satellites such as the Self-Calibrating Multivariate Precipitation Retrievals (SCaMPR) can help address spatial gaps by providing continuous spatial coverage (Scofield and Kuligowski 2003). This advantage of satellite QPE's has led to their incorporation into the

3

Multisensor Precipitation Estimation algorithm (Kondragunta et al. 2005). Potential applications of near real-time satellite QPEs for disaster preparedness and mitigation are possible at both regional and global scales (Hong et al. 2007).

The relationship between the satellite retrieved IR brightness temperatures of storms and precipitation rates at the surface has been well documented especially for convection, and methods utilizing IR brightness temperatures to estimate precipitation have been developed and modified over the last three decades (e.g., Negri and Adler 1981; Adler and Negri 1988; Vicente et al. 1998). The current operational satellite rainfall estimation algorithm at the NOAA National Environmental Satellite, Data, and Information Service (NESDIS) is the Hydro-Estimator (H-E), which estimates precipitation from geostationary platforms by relating IR brightness temperatures to precipitation rates (Kuligowski and Scofield 2003). The next-generation operational NOAA / NESDIS algorithm for GOES-R, the Self-Calibrating Multivariate Precipitation Retrieval (SCaMPR) employs IR brightness temperature and microwave data (Kuligowski 2010). Numerous other real-time algorithms exist for retrieving rainfall rates from IR and microwave data, including the Climate Prediction Center Morphing algorithm (CMORPH; Joyce et al. 2004), Global Satellite Mapping of Precipitation (GSMaP_MVK+; Kubota et al. 2007), the Naval Research Laboratory (NRL) Blended algorithm (Turk et al. 2003), Precipitation Estimation from Remotely Sensed Information using Artificial Neural Networks (PERSIANN; Sorooshian et al. 2000), and the Tropical Rainfall Measuring Mission (TRMM) Multi-sensor Precipitation Algorithm (TMPA; Huffman et al. 2007). However, this study will

focus on evaluating and improving SCaMPR in preparation for its operational application at NOAA / NESDIS after the GOES-R launch. With the launch of GOES-R, the full version of the SCaMPR algorithm will be run, and it's output incorporated into the Advanced Weather Interactive Processing System for use by NWS forecasters.

Improving Satellite QPEs

To improve satellite derived QPEs during DCSs a source of validation data is needed with significantly better spatial and temporal coverage and resolution than rain gauge networks provide. Recent studies such as Kirstetter et al. (2012) and Amitai et al. (2012) have utilized ground-based radar estimates as a validation source for the Tropical Rainfall Measurement Mission (TRMM). Even more detailed validation and analysis can be achieved using a combination of NEXRAD observations and GOES satellite retrievals to classify the three components of a DCS (Feng et al. 2011, 2012), which provides guidance to improve the spatial precipitation characteristics of satellite QPEs such as SCaMPR. Since the size of the anvil area of a DCS is highly variable, and the IR brightness temperatures over anvil regions are similar to those over convective cores (Feng et al. 2011, 2012), effectively separating anvil from raincore regions prior to calculating IR based precipitation rates could significantly improve geostationary satellite QPEs (Vicente et al. 1998). Using a combination of the National Mosaic and Multi-sensor Quantitative Precipitation Estimation System (NMQ) Q2 and GOES data, DCSs can be broken into three components which allow better evaluation of the strengths and weaknesses of SCaMPR retrievals. Findings from these evaluations could eventually improve separation

5

of anvil and raincore regions using only geostationary satellite retrievals. However, the uncertainties and errors in radar-derived Q2 estimates and satellite-derived precipitation products must first be properly analyzed and validated with ground-based rain gauge measurements that can provide independent "ground truth" for validations.

Many uncertainties involved in radar precipitation estimates and attempts to mitigate these uncertainties have been discussed in previous studies (Andrieu et al. 1997; Austin 1987; Langston et al. 2007; Villarini and Krajewski 2010; Smith et al. 1996; Zhang et al. 2005; Zhang and Qi 2010; Zhang et al. 2011). In a recent evaluation of NMQ and the Precipitation Processing System (PPS) over the conterminous United States (CONUS), Wu et al. (2012) found that NMQ estimates performed better on average than the PPS over the CONUS and during heavy precipitation events. While the findings of Wu et al. (2012) and Chen et al. (2013) support the use of NMQ Q2 estimates as the primary data set for improving satellite QPEs, an evaluation of the magnitude of NMQ Q2 errors and their biases over longer time periods are necessary against a more dense rain gauge network in a region where precipitation is largely from DCSs. Furthermore, although the distribution of precipitation among different Z-R regimes has been studied (Chen et al. 2013), analysis of the distribution of estimated precipitation into DCS regions is needed to quantitatively examine the errors and biases of satellite QPEs.

Recently, the NWS has upgraded its radar network to include dual polarization technology. Dual polarization radar allows transmitting in both the horizontal and vertical directions, providing more information about targeted hydrometeors than a radar utilizing

only one beam orientation provides. Thorough overviews of dual polarization are already available in literature (Islam and Rico-Ramirez 2013), so only a brief summary of dual polarization applications to the hybrid classification (Feng et al. 2011) and Q2 estimates will be discussed in this study. While the Q2 algorithm utilizes only horizontal polarization, some incorporation of dual polarization technology could aid in removing ground clutter contamination of estimates (Zrnic et al. 2006). In the next generation version of Q2, Q3, dual polarization data (hydrometeor classification algorithm output (Park et al. 2009)) will be used for precipitation type determination and removal of non-meteorological returns from precipitation estimates. This incorporation of dual polarization data should greatly improve the performance of Q2 in frozen precipitation events and events where temperature inversion induced ground clutter causes estimates of erroneous light precipitation. Additionally, hail core classifications could be added to the current hybrid classification algorithm developed by Feng et al. (2011) by utilizing the hydrometeor classifications developed for the WSR-88D (Park et al. 2009). As hail cores are a significant part of DCSs, this revised classification algorithm would allow a more detailed examination of DCS structures and their life cycles.

Purpose

To evaluate both NMQ Q2 estimates and SCaMPR retrievals in a region with precipitation dominated by DCSs, OK MESONET observed precipitation has been used as ground truth in this study. This study will use timescales from 24-hr precipitation to annual precipitation to examine the performance of retrievals and estimates for both individual

precipitation events and longer timescales. The NMQ Q2 estimates during the period 2010-2012 will be directly compared to collocated OK MESONET observations to determine the accuracy, consistency, and any biases associated with Q2 estimates. The same direct collocation analysis will be performed on SCaMPR for 2012 data to evaluate the performance of SCaMPR retrievals and possible sources of error. Daily through yearly timescales will be analyzed to evaluate performance ranging from individual events to annual estimates. Potential causes for any biases or errors will be examined along with possible methods of improvement. Special attention will be given to the absolute accuracy of Q2 estimates and scenarios where SCaMPR retrievals produced significant overestimates. Additionally, precipitation distributions will be calculated for each of the DCS regions from both observations and estimates. This will provide a quantitative insight into the precipitation characteristics of DCSs, while also evaluating the accuracy of both Q2 and SCaMPR precipitation estimates in providing reasonable precipitation distributions for DCSs. By examining the estimated precipitation distribution from SCaMPR, the cause of errors can be diagnosed and more precisely accounted for and corrected than using only qualitative studies. Furthermore, an evaluation of the estimated precipitation distribution from Q2 can determine how reasonable a substitute for ground truth this product is where dense rain gauge networks are unavailable.

By evaluating the performance of both SCaMPR and Q2, this study will explore potential pathways for improvements of satellite QPEs during DCSs in a more targeted approach than previous studies. The accuracy of Q2 in a region with annual precipitation

dominated by convection will first be examined to determine how reliable of a substitute Q2 estimates can be for calibrating satellite QPEs when a higher resolution validation data set is needed than rain gauge networks provide. Next, SCaMPR estimates will be evaluated on multiple temporal and spatial scales to pinpoint the sources of bias and error for this IR-based satellite QPE. Lastly, a new algorithm to identify precipitating areas solely from GOES data will be developed and tested. A discussion of these findings and preliminary results from the newly developed method to correct the biases/errors of SCaMPR will be provided.

CHAPTER II

DATA AND METHODOLOGIES

NEXRAD Q2 Data

The NMQ Q2 Tile 6 estimates from January 2010 through December 2012 were compared with OK MESONET observations and SCaMPR retrievals. NMQ Tile 6 is bounded longitudinally by 110ºW and 90ºW, and has northern and southern boundaries at 40ºN and 20ºN as shown in Figure 2.
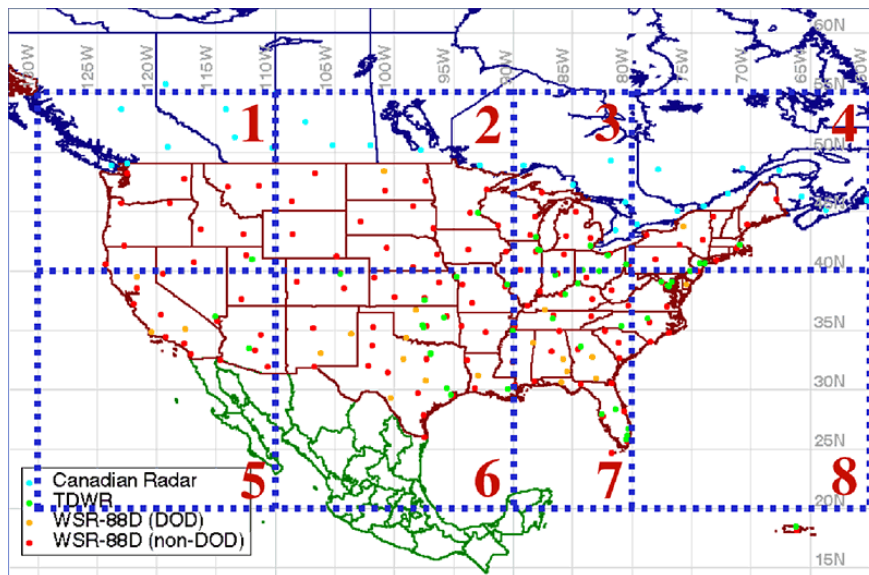
Figure 2. The NMQ domain and tiles, the boundaries of the tiles are indicated by blue dashed lines.
Source: http://www.nssl.gov/projects/q2/tutorial/3dmosaic.php

As there is no available radar data below 25° N as shown in Figure 2, only data northward

from 25° N was used in this study.

NMQ Q2 estimates provide multi-radar precipitation estimates with a grid box of

1km x 1km [http://www.nssl.noaa.gov/projects/q2/q2.php]. Q2 estimates are produced

using quality controlled radar reflectivity data from multiple radars to automatically

classify precipitation as convective rain, stratiform rain, warm rain, hail, and snow (Zhang

et al. 2011). The rules of the classification system are shown in Figure 3.
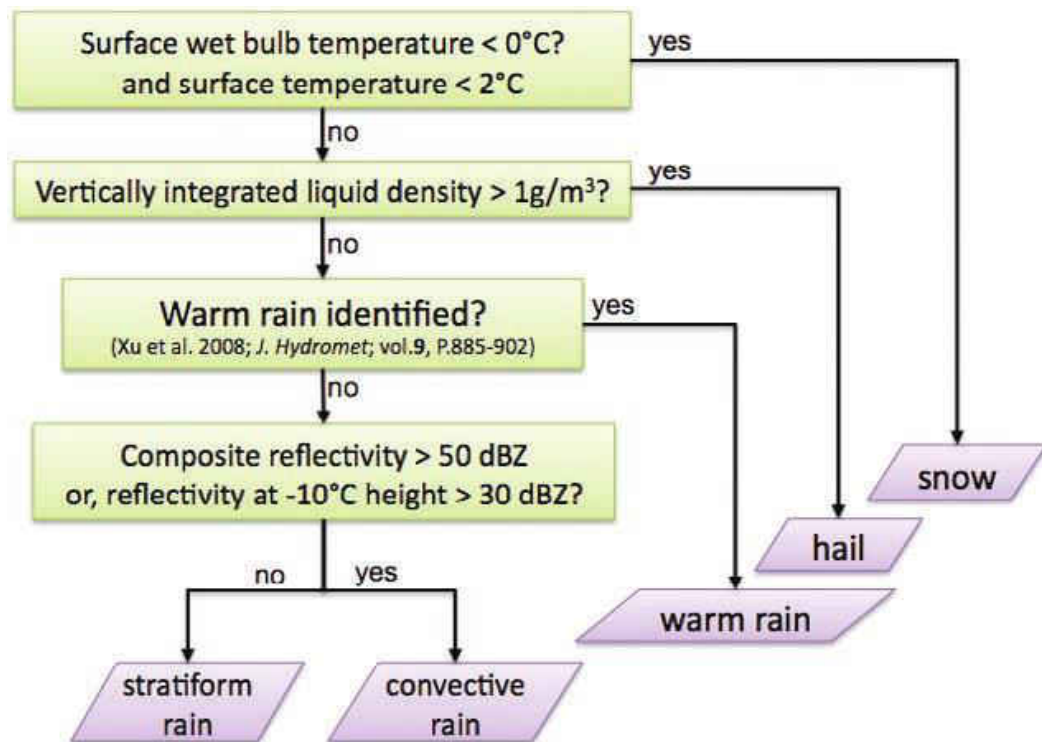
Figure 3. The precipitation classification process used in the Q2 algorithm. Source:
Fig. 9 of Zhang et al. 2011

Each classification of precipitation has a Z-R relationship assigned to it as shown in Figure 4.
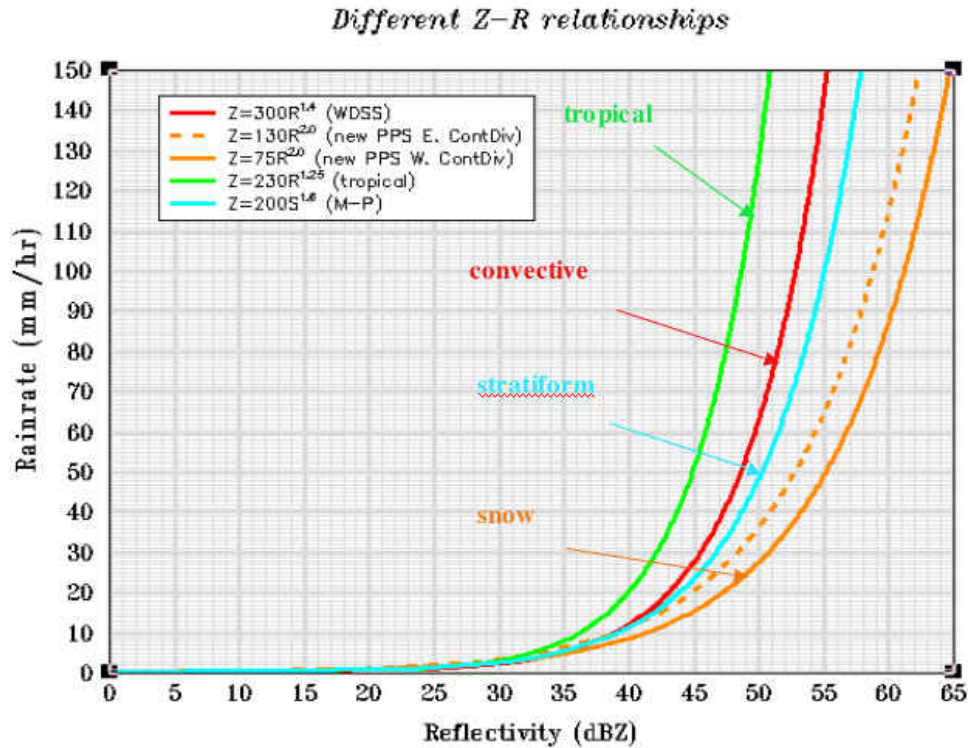
Figure 4. The different Z-R relationships used by the Q2 algorithm for the four classifications of precipitation.
Source: (http://www.nssl.noaa.gov/projects/q2/tutorial/q2.php)

These assigned Z-R relationships based on precipitation classification are used for each radar pixel to provide the Q2 estimated rain rates (Zhang et al. 2011). These pixel-level estimates can easily be compared to collocated OK MESONET observations by determining which pixels each MESONET station is located in.

The large spatial coverage and high spatial resolution of the NEXRAD Q2 estimates will provide a means assessing (and potentially improving) the performance of the SCaMPR retrievals over large areas with a much finer resolution than rain gauge networks.

OK MESONET

Oklahoma MESONET 24-hour accumulated precipitation from January 2010 through December 2012 was used as ground truth in this study. Additionally, 5-minute accumulated precipitation observations were used during selected convective events in 2012. An unheated tipping bucket with an alter shield to minimize wind effects is used at each of the MESONET stations as shown in Figure 5.

Figure 5. An unheated tipping bucket with alter shield that is used for OK MESONET precipitation observations.

Each tip of the tipping bucket occurs when 0.25mm (0.01") of precipitation is collected. There are a total of 119 MESONET stations with data spanning the entire time period for this study. Since the gauges are unheated, measurements of frozen precipitation are unreliable and can cause time mismatches between observed and falling precipitation. However, potential time mismatch problems during frozen precipitation events were minimal because frozen precipitation typically accounts for ~1% of annual precipitation in the study region.

SCaMPR Retrievals

The GOES-R algorithm for rain detection and estimation, SCaMPR, attempts to capture the accuracy of microwave (MW) rain rates along with the rapid refresh of GOES data by calibrating GOES IR-based predictors against MW rainfall (Kuligowski 2010). Separately matched data sets for four latitude bands and three cloud types (determined using brightness temperature differences between bands) are updated every time new MW rain rates become available and the oldest data are removed. Whenever the matched data sets are updated, discriminant analysis is used to identify the two best predictors and coefficients for discriminating raining from non-raining pixels; stepwise forward linear regression is used to select the two best predictors and coefficients for deriving rain rates. To account for the nonlinear relationship between IR brightness temperatures and rain rates, the former are regressed against the latter in log-log space to produce additional rain rate predictors. To compensate for the compression of the statistical distribution which results from applying regression techniques to non-normally distributed data, the

cumulative distribution functions (CDFs) of the rain rates derived via regression from dependent data are matched against the CDFs of the MW rain rates to create a lookup table that restores the retrieved rain rates to the correct distribution. Additional details on the SCaMPR algorithm are available in Kuligowski (2010).

The full version of SCaMPR was developed using five bands from the METEOSAT Spinning Enhanced Visible InfraRed Imager (SEVIRI)—the water vapor bands at 6.2 and 7.3 µm and the IR window bands at 8.7, 10.8, and 12.0 µm. However, the version of SCaMPR evaluated in this paper was simplified from the full version because only two of the five bands used by the algorithm are available on current GOES—one water vapor band at 6.7 µm and one IR window band at 10.7 µm; among other changes, this meant that only two cloud types existed instead of three and the available predictor data set was reduced by half. SCaMPR precipitation retrievals were only available from January 2012 through December 2012 and during the Midlatitude Continental Convective Clouds (MC3E) campaign in 2011, with a grid box of 4km x 4km, and a domain bounded by the coverage of GOES East and GOES West. For this study only complete coverage of Oklahoma was necessary, but the SCaMPR domain covers the entire CONUS as shown in Figure 6.

A modified version of the SCaMPR algorithm, SCaMPR RH was also available for 16 days with convective activity during 2012. All of the details of this algorithm are the same as SCaMPR, except that SCaMPR RH incorporates modeled relative humidity, RH, and one of the predictors. The modeled RH input will allow reduction of SCaMPR

estimated precipitation rates in regions with a significant dry layer that precipitation must fall through prior to reaching the ground.
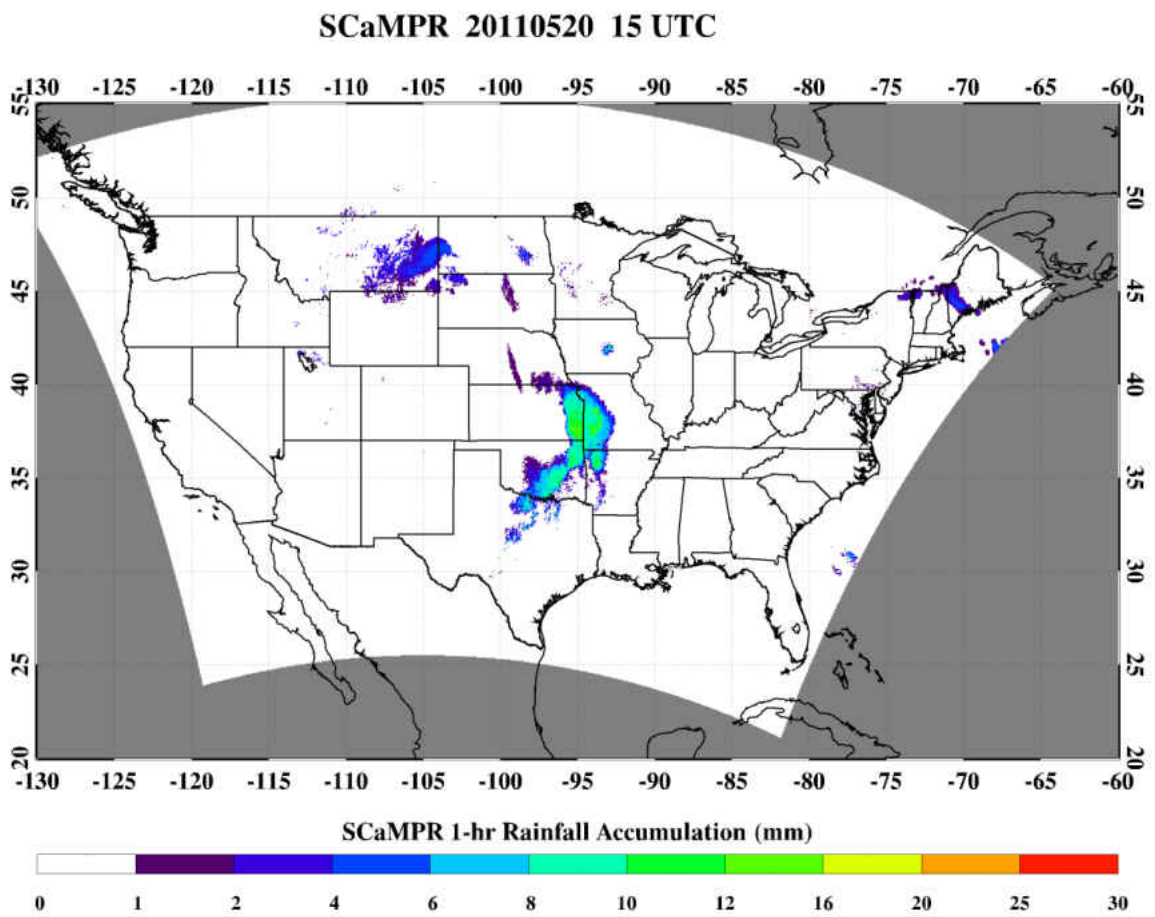
Figure 6. Image of SCaMPR domain for precipitation estimates over the CONUS. Estimate of precipitation accumulated in the hour ending 15 UTC 20 May 2011 is shown.

GOES Retrievals

GOES retrievals for cloud top brightness temperatures and cloud optical depth were provided by NASA Langley. Retrievals were provided on a grid with approximately 4km x 4km grid boxes using the Visible Infrared Solar-Infrared Split Window Technique (VISST) algorithm (Minnis et al. 2011). Cloud optical properties are calculated by matching parameterizations of theoretical radiance calculations for both water and ice crystal size distributions to measurements. These retrievals were again bounded by the domains of GOES East and GOES West, but only a smaller subset of data was focused on as shown in Figure 7. Cloud optical depth retrievals are valid during
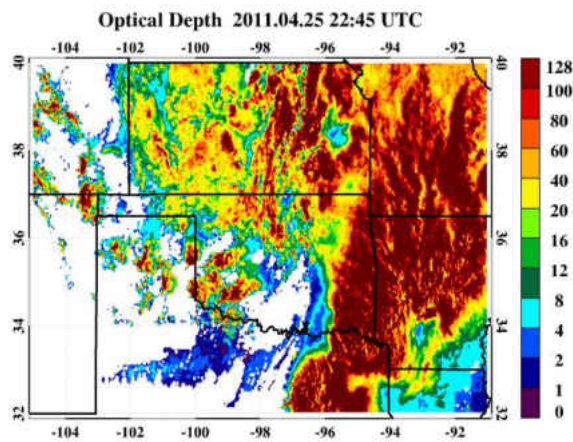
Figure 7. Optical depth over the SGP region on 25 April 2011.

daylight hours, but not near dusk and dawn as the solar zenith angle at these times produces too great of errors in the radiance calculations. These optical depth retrievals have a maximum value of 128 prior to 2012, and 150 for 2012.

Methodologies

When evaluating NMQ Q2 estimates and SCaMPR retrievals, OK MESONET observations were treated as ground truth. After determining which pixels on the NMQ and SCaMPR grids corresponded with the MESONET locations, the NMQ Q2 estimates and SCaMPR retrievals were directly compared to collocated MESONET observations. Comparisons were only made when both data sets were available, such as Q2 vs. MESONET during 2010-2012 and SCaMPR vs. MESONET in 2012.

Scatterplots were constructed between the Q2 estimates and MESONET observations when MESONET observations had recorded precipitation (≥0.25 mm, the minimum detectable value for the MESONET rain gauges). Regression lines were derived for two spatial scales: (1) the 24-hour accumulated and annual precipitation from each MESONET station, and (2) the statewide 24-hr total precipitation from all MESONET stations. Since radar coverage variation has been well documented over the U.S. (Maddox et al. 2002), this study was also performed only for those MESONET stations in regions of good radar coverage; that is, the bottom of the radar base beam was ≤1219 m AGL (generally within ~130 km of the radar location).

Additionally, comparisons between the Q2 estimates and MESONET observations were made for both the warm and cold seasons. The warm season was defined as April through September, while the cold season was from October through March (Wu et al. 2012). These seasons help broadly separate precipitation characteristics to evaluate the

accuracy of Q2 estimates for strong convection and weaker convection/stratiform-dominated precipitation regimes. Scatterplots were created for 24-hr precipitation estimates and observations during both the warm and cold seasons along with their corresponding linear regression equations. The same comparison between the SCaMPR retrievals and MESONET observations was done only for 2012.

In addition to regressing the Q2 estimated and SCaMPR retrieved precipitation against MESONET observations, cumulative frequency distributions were constructed for each of the data sets. To construct the cumulative frequency distributions, a total of 50 2-mm bins were generated from all available samples for each data set. Bar graphs comparing the cumulative frequency distributions were also created by subtracting the percentages of precipitation events in each MESONET bin from the percentages in the collocated Q2 estimate or SCaMPR retrieval bins. These bar graphs allow the visualization of distribution differences, which provide additional information regarding the slope of the cumulative frequency distributions. Finally, categorical scores were calculated for both NMQ Q2 estimates and SCaMPR retrievals using four thresholds of MESONET rainfall accumulation for the false alarm rate (FAR), probability of detection (POD), and critical success index (CSI). The categorical scores are calculated as follows; POD is defined as the ratio of hits to the sum of misses and hits. Each hit represents an occurrence of an estimate greater than the threshold value when MESONET observed precipitation also exceeds the threshold value. A miss represents an occurrence of an estimate less than the threshold value when MESONET observed precipitation exceeds the threshold

value. FAR is defined as false alarms divided by the sum of false alarms and hits. A false alarm represents an occurrence of an estimate greater than the threshold value when MESONET observed precipitation did not exceed the threshold value. Lastly, CSI is defined as the ratio of hits to the sum of hits, misses, and false alarms. The threshold values were 0.25mm, 2.5mm, 12.5mm, and 25mm for 24-hr accumulated precipitation events spanning three years of NMQ Q2 estimates and one year of SCaMPR retrievals. Root-mean square error (RMSE) values were calculated for 24-hr precipitation events with four threshold values. Only the lowest bound of 0 mm (not 0.25mm) differed from the threshold values above to quantify the errors of precipitation estimates when none was observed. Additionally, RMSE scores were calculated for the annual average, and for 2012 when both SCaMPR and Q2 data were available.

To address the precipitation characteristics of DCSs and to evaluate Q2 and SCaMPR performance in DCSs, precipitation distributions were calculated from MESONET observations and from SCaMPR and Q2 estimates. DCS components (CC, SR, and AC) were classified using NEXRAD and GOES data (Feng et al. 2011, 2012) over OK. All SCaMPR and Q2 pixels were matched with the classified components, and their corresponding precipitation distributions were then calculated based on the sum of rates for each classified pixel. For the MESONET precipitation distribution, the classification over each MESONET station was matched with the 5-minute accumulated precipitation ending at the time of the classification. There was little sensitivity between choosing the 5-minute accumulation starting/ending at the time of the DCS classification.

Development of New Algorithm

A new algorithm was created to incorporate both cloud optical depth and cloud top brightness temperatures to reduce erroneous precipitation retrievals from the SCaMPR algorithm. After discovering the tendency of SCaMPR to dramatically overestimate precipitation in anvil regions because AC and CC regions share similar cloud top brightness temperatures, a method to separate AC from raincore regions was developed using cloud optical depth. As a significant difference in optical depth is present between raincore and AC regions as shown in Figure 8,
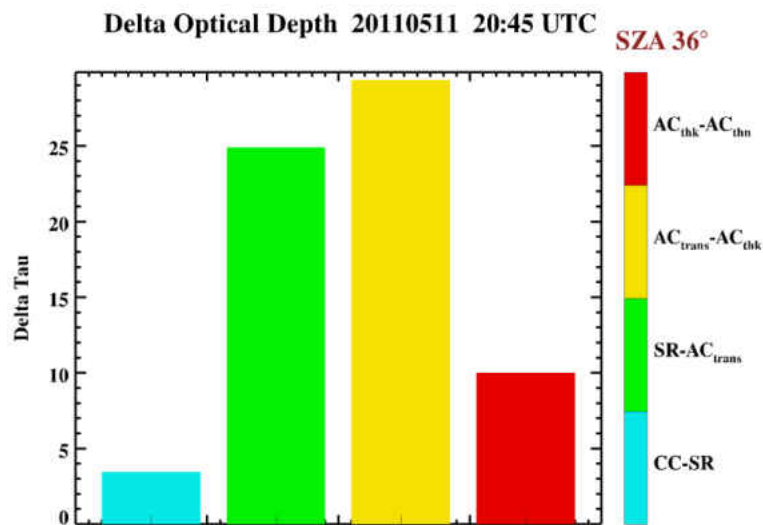
Figure 8. Average optical depth difference between different DCS regions for 11 May 2011 at 2045 UTC.

optical depth can be used to effectively separate precipitating and non-precipitating regions of DCSs when combined with cloud top brightness temperature retrievals.

This new algorithm was developed from both physical characteristics of precipitation in DCSs and observed empirical relationships between cloud optical depth, cloud top BTs, and precipitation. First, the cloud top BT and cloud optical depth of each pixel is screened to identify potential rain cores. A rain core represents a pixel with an optical depth large enough and a cloud top BT temperature low enough to expect precipitation. Depending on the cloud top BT temperature, a radius of influence is assigned to each rain core. A colder cloud top BT will increase the radius of influence, and a pixel with a colder cloud top BT and a high cloud optical depth value likely contains or is close to a CC region.

The optical depth threshold set for raincores in this algorithm is 90. The first temperature threshold is 273 K, the freezing level. A total of five temperature thresholds are used, and a corresponding radius of influence is set to each identified rain core such that all pixels within the radius of influence will be identified as raining. The different threshold levels are detailed in Table 1.

Table 1. Overview of new algorithm using cloud top BT and cloud optical depth to identify precipitating pixels.

BT of Pixel (K)	Cloud Optical Depth of Pixel	Pixels in Square Defined as Precipitating
273 > T > 250	>90	9
250 > T > 220	>90	25
220 > T > 215	>90	49
215 > T > 210	>90	81
210 > T	>90	121

Pixels in the radius of influence create a square, with the rain core pixel as the center pixel of the square. In Figure 9 it is shown that the side length of the square will be increased by 2 pixels for each successive threshold with colder cloud top BTs.

The sensitivity of estimated precipitating area to changing the optical depth threshold to identify rain cores was not particularly strong. Increasing or decreasing the tau threshold value by ~10 % reduced or increased the estimated precipitating area by ~ 5 %. A higher optical depth threshold limits the FAR, but at the expense of POD, while a lower optical depth threshold will maintain a high POD, while allowing FAR to be
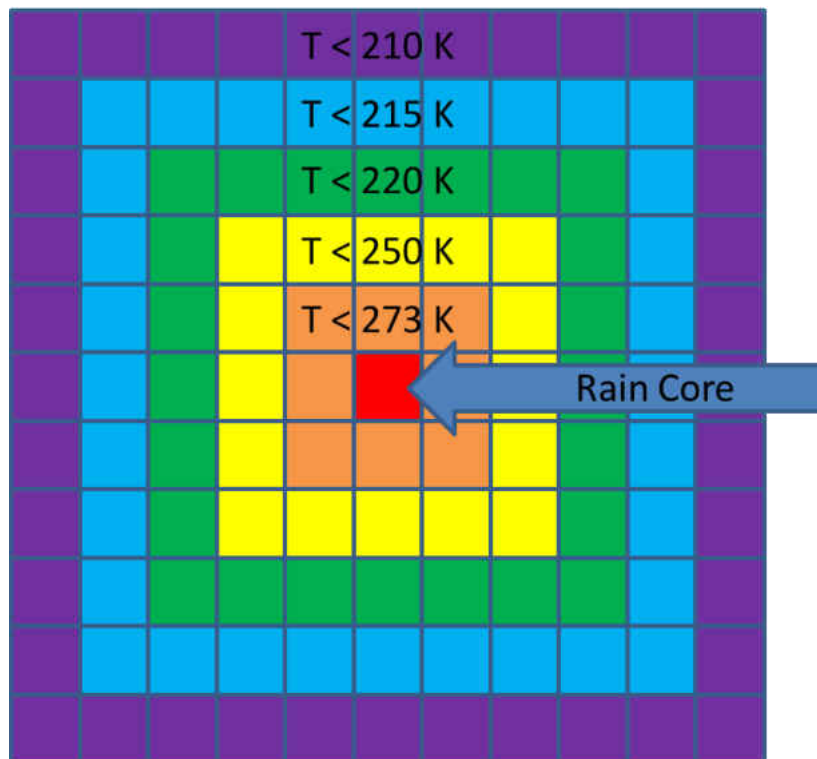
Figure 9. Each color represents additional pixels that will be identified as precipitating if the cloud top BT of the rain core pixel(optical depth > 90) falls below the temperatures indicated. For example, all yellow pixels will be identified as precipitating if the cloud top BT of the rain core pixel is less than 250K.

23

slightly larger. However, even for very low tau thresholds, ~35, the FAR is still

significantly improved over the SCaMPR algorithm. The threshold of 90 used in this

study was chosen because qualitatively it produced a reasonable precipitating area while

greatly reducing FAR. For operational uses, the tau threshold will likely be reduced

significantly to keep the POD as large as possible. Additionally, as lowering the tau

threshold still allows significant reductions in FAR over the SCaMPR algorithm this will

likely be the preferred version of the algorithm. Further objective evaluation is needed to

determine the optimal tau threshold for an operational version of this algorithm.

Physically, this algorithm represents the increased probability of precipitation

occurring near a pixel with a large cloud optical depth and cold cloud top BTs. Since

precipitation in DCSs is possible from clouds with optical depth values below 90, this

algorithm accounts for that while still ensuring pixels identified as precipitating are near

raincore regions. Pixels identified as precipitating can have optical depth values less than

90 as long as they are within the radius of influence of a pixel meeting the criteria defined

for a raincore. While this algorithm does make the assumption that the precipitating area

of convective systems is symmetrical, in qualitative studies there does not appear to be a

significant upshear or downshear bias present. Although it is possible the precipitating

area could be overestimated on the upshear side of convection and underestimated on the

downshear side of convection by assuming symmetry, no significant biases have yet been

detected. A more detailed analysis, and possible incorporation of modeled wind fields to address this potential concern could be examined in future studies.

To evaluate the performance of this algorithm compared to SCaMPR in properly identifying the precipitating regions of DCSs, two methods were used. First, the total percentage of precipitating area was calculated for SCaMPR, Q2, and the new algorithm. This analysis was based on hourly precipitation estimates during the MC3E campaign. To ensure a fair comparison, the new algorithm was run only on data available to produce the SCaMPR hourly estimates, while Q2 estimates were based on instantaneous estimates available at the times of GOES images used by SCaMPR and the new algorithm. The total percentage of precipitating area for NMQ tile 6 was calculated during daylight hours for the entire MC3E campaign.

Secondly, with SCaMPR instantaneous estimates available in 2012, the distribution of precipitation among the DCS components was calculated for SCaMPR, Q2, and the two versions of SCaMPR with the new algorithm applied. In addition to comparing the estimated precipitation distributions between these datasets, the estimated size of precipitating anvil regions were calculated and compared. By examining the estimated distribution of precipitation among DCS components with the new algorithm applied to SCaMPR as well as the size of the estimated precipitating anvil regions, the success of the new algorithm in reducing anvil area overestimates could be evaluated.

CHAPTER III

RESULTS

Q2 vs. OK MESONET

Figure 10 shows the scatterplots of 24-hr accumulated precipitation from collocated OK MESONET observations and Q2 estimates during the period 2010-2012. There are a total of 27,201 samples when precipitation was recorded by a MESONET station (≥0.25 mm) and Q2 estimates were available. A linear relationship between the two datasets was found, providing a strong correlation of 0.881. On average, Q2 estimates were about 25.6% higher than MESONET observations (Fig. 10a), mainly because of contributions by the warm season (April – September) when Q2 estimates had a positive bias of 37.9% (Fig. 10b). During the cold season (October through March), however, an excellent agreement (~5%) was reached between the two data sets (Fig. 10c). The sample sizes during the warm and cold seasons were nearly equal and their correlations were also similar. There were more intense precipitation events during the warm season than during the cold season; as a result, the mean 24-hr accumulated precipitation from MESONET observations increased from 7.42 mm to 10.66 mm (43.7%) from the cold to warm season, while Q2 estimates increased from 7.81 mm to
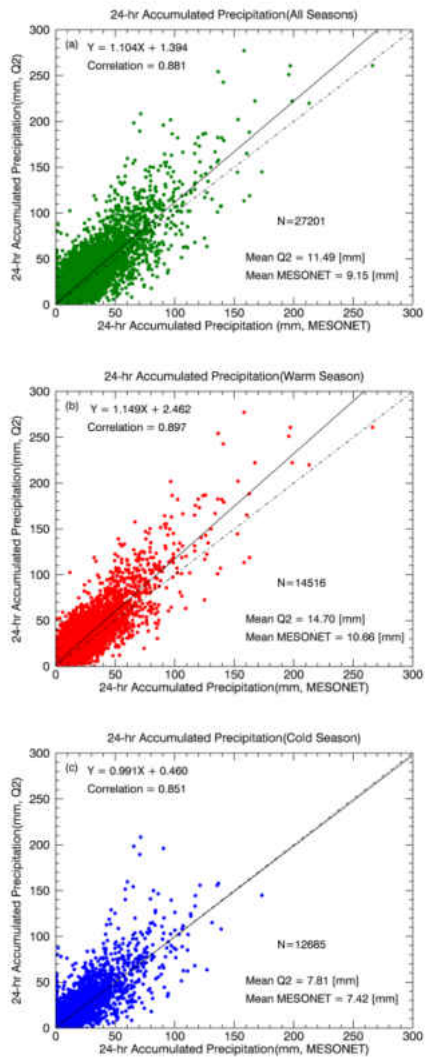
Figure 10. Each colored dot represents a pair of collocated MESONET observed and Q2 estimated 24-hr accumulated precipitation (rainfall > 0.25 mm; i.e., excluding non-precipitating events at each MESONET station) during the period 2010-2012. Shown are (a) all available collocated MESONET and Q2 observations, (b) the warm season (April through September), and (c) the cold season (October through March).

14.70 mm (88.2%). The excellent agreement during the cold season indicates that the Q2

precipitation estimates from NEXRAD reflectivity are reasonable for stratiform dominated

27

precipitation. The Q2 estimated precipitation during the warm season, however, produced

overestimates. These overestimates are likely attributed to incorrect classifications of

tropical rain in the Q2 algorithm (Chen et al. 2013) and possibly from increased reflectivity

due to hail and graupel (Wu et al. 2013).

Figure 11 compares the Cumulative Frequency Distributions (CFDs) with a total of

125,543 collocated Q2 estimates and MESONET observations during the 3-yr period.
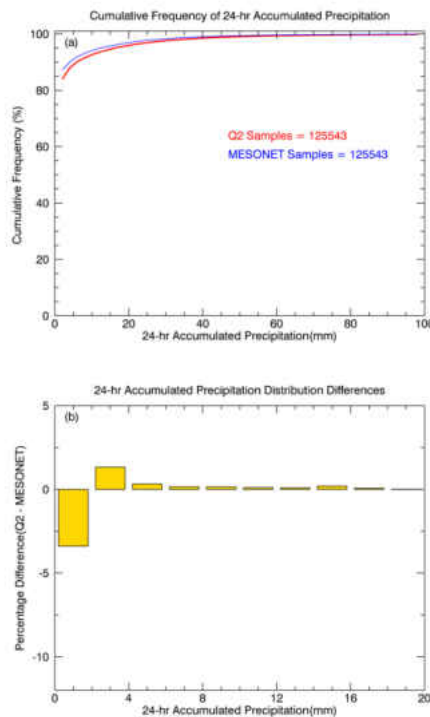
Figure 11. (a) Cumulative frequency of 24-hr accumulated precipitation from all samples (rainfall ≥ 0 mm) during the period 2010-2012. Both MESONET and Q2 samples were sorted into fifty 2-mm bins. (b) The percentages of the samples of each bin to total samples (3 years * 365 days * 119 stations) for both MESONET and Q2 are calculated, respectively, and their percentage differences (Q2-MESONET) for each bin are calculated until bin 10 (up to 20 mm; after that the percentage differences are negligible).

As opposed to the samples in Fig. 10 (rainfall ≥ 0.25 mm), the total samples in Fig. 11 include all collocated Q2 estimates and MESONET observations; i.e., non-precipitating events are included in Fig. 11. These samples were sorted into 50 2-mm bins where both MESONET and Q2 CFDs were dominated by their first bin (0-2 mm, ~85%) because the non-precipitating events were included in this bin. Both CFDs approached 100% with very similar slopes as the precipitation amounts of the bins increased (Fig. 2a). The corresponding percentages of the samples in each bin to total samples (~3 years * 365 days * 119 stations) for both MESONET and Q2 were calculated first, and then their percentage differences (Q2-MESONET) for each bin were calculated and shown in Fig. 2b. The largest difference occurred in the first bin, 0-2mm, where the Q2 percentage was 3.2% lower than the MESONET percentage (Fig. 11b). This suggests that Q2 overestimated precipitation for light rain events compared to MESONET observations because the distribution is shifted towards higher precipitation amounts for Q2 estimates. For other bins, the Q2 percentages were slightly higher than the corresponded MESONET percentages and the differences became negligible as the precipitation amounts of the bins increased (Fig. 11b).

To evaluate the spatial average of 24-hr accumulated precipitation, statewide 24-hr total precipitation, the sum of all MESONET observations (collocated Q2 estimates), are plotted in Fig. 12.
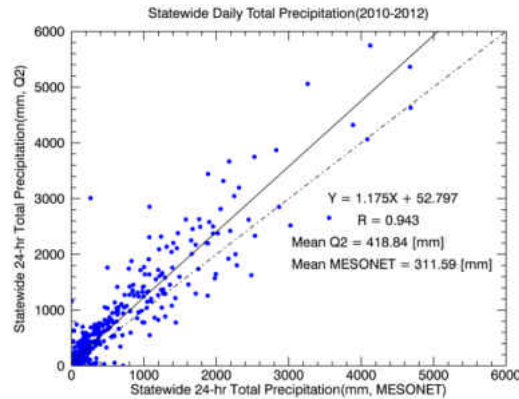
Figure 12. Each blue dot represents 24-hour total precipitation (statewide rainfall ≥ 0.25 mm; i.e., excluding non-precipitating events) from all OK MESONET stations and collocated Q2 estimates during the period 2010-2012 (N=798).

This comparison only includes precipitation events (at least one MESONET station recorded 24-hr total precipitation ≥ 0.25 mm). Similar to the analysis of the individual gauge values in Fig. 1a, a linear relationship between the two data sets was found with a stronger correlation of 0.943 (vs. 0.881 in Fig. 10a), which would be expected from a statewide total precipitation with less temporal variability than the individual gauges. Again, Q2 estimates, on average, were higher than MESONET observations by 34.4% in this comparison. Two outliers appeared in Fig. 3 where the Q2 estimates were 1219 mm and 3000 mm, while the corresponding statewide MESONET observations were nearly zero and less than 400 mm, respectively. Further examination into these two outliers using data from the National Climatic Data Center (NCDC) revealed that both outliers occurred during heavy snowfall events over OK. Since the MESONET gauges were unheated, they

30

were not able to record the falling frozen precipitation during these two events. Removal of these outliers from the analysis produces negligible changes in the results.

To further investigate the temporal averages of 24-hr accumulated precipitation at each MESONET station, the average annual precipitation distributions for both MESONET and Q2 over the entire state of OK during the period 2010-2012 is presented in Fig. 13. As illustrated in Fig. 13, MESONET observations varied from ~300 mm in western OK to slightly over 1000 mm in eastern OK (Fig. 13a), whereas Q2 estimates reached around 1500 mm in eastern OK (Fig. 13b). Mean Q2 precipitation estimates over the state of OK exceeded mean MESONET observed precipitation by 242.4 mm (~35.1%) (Fig. 13c). Q2 estimates were higher than MESONET observations across most of OK with a few notable exceptions. In extreme southeastern OK, the western panhandle, and northwestern OK to the northeast of the Texas panhandle, Q2 estimates were significantly less than MESONET observations (Fig. 13c). The Q2 underestimates over these two regions are primarily due to poor radar coverage shown in Fig. 14. The regions of significant underestimates are located where the bottom of the base beam height is greater than 1219 m above ground level and in some cases exceeds 3000 m AGL (Fig. 14). With the volume scans overshooting much of the falling precipitation in these regions, underestimates occur.
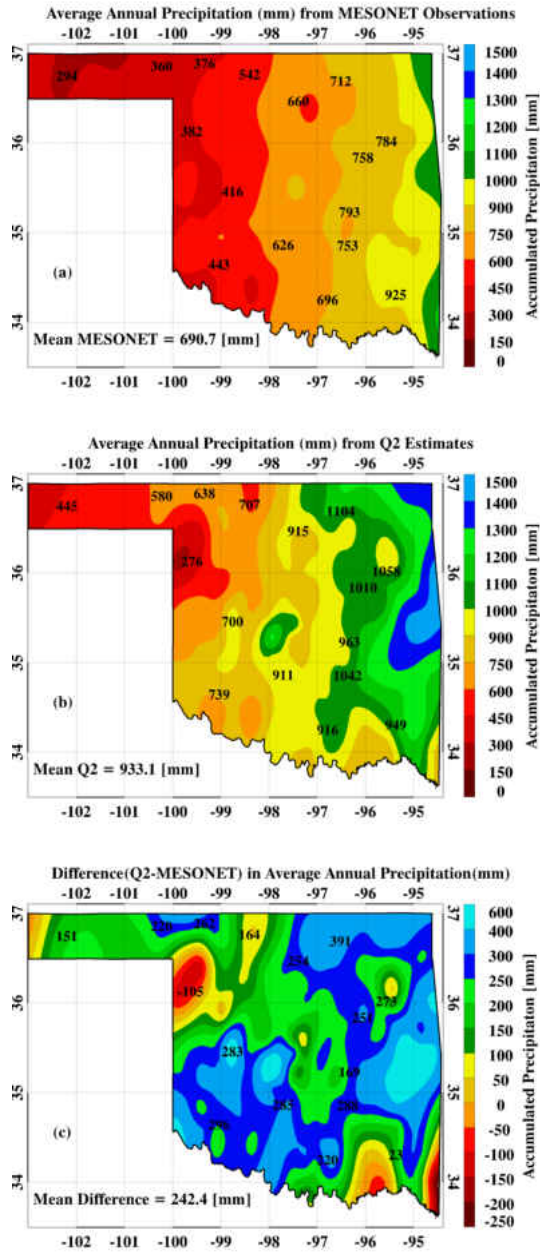
Figure 13. Average annual precipitation (a) observed by the Oklahoma MESONET stations, (b) estimated by NEXRAD Q2, and (c) their difference (Q2-MESONET) during the period 2010-2012.
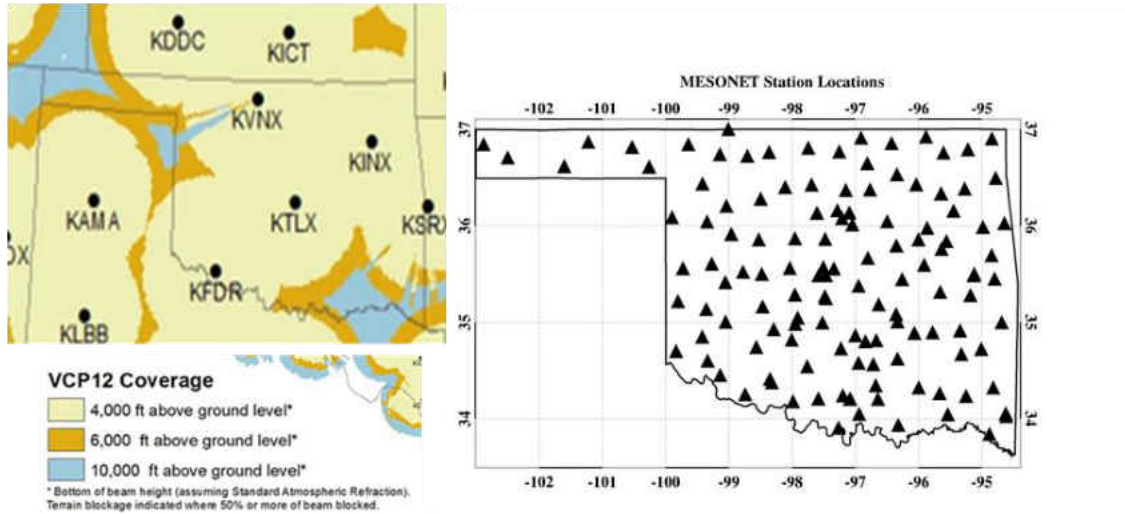
Figure 14. Image of NEXRAD radar coverage provided by NOAA's NWS Radar Operational Center. Bottom of base beam height assuming standard atmospheric refraction is contoured for Volume Coverage Pattern 12 scans. Light yellow color (good radar coverage in this study) represents coverage with the bottom of base beam height ≤ 4000 ft (1219 m), orange color represents > 4000 ft and ≤ 6000 ft (1829 m), and light blue represents > 6000 ft and ≤ 10,000 ft (3048 m). Location of all MESONET stations represented by black triangles (right).

Figure 15 presents the same scatterplot as Fig. 10 except for the samples with good radar coverage. Compared to the results in Fig. 10, the correlations are slightly stronger and the means are slightly higher in Fig. 15. The largest increases in correlation (+.019) and wet bias (+5.84%) occurred during the cold season, while those during the warm season only increased slightly. It is likely the Q2 estimates during the cold season were impacted more by radar coverage than those during the warm season because precipitating clouds tend to be more shallow (more likely to be overshot by radar) during the cold season.

The impacts of radar coverage on Q2 estimates on an annual time scale are shown by scatterplots of average annual precipitation from collocated MESONET observations and Q2 estimates at each MESONET station in Fig. 16.
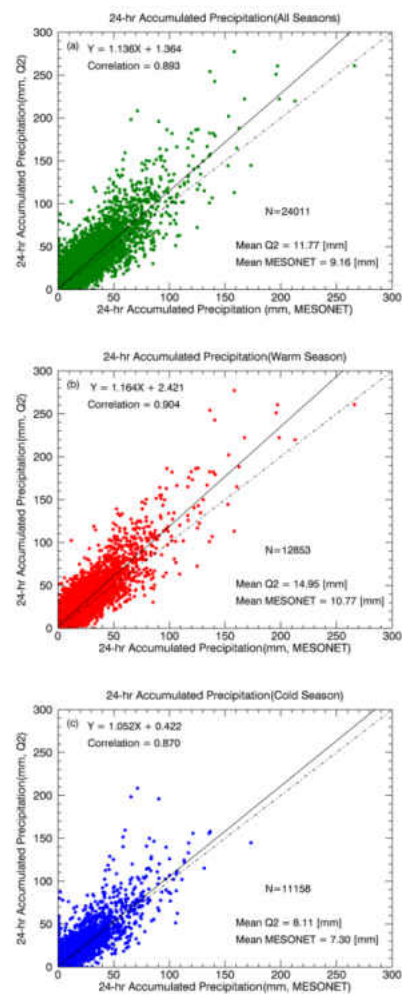
Figure 15. Same as Fig. 10 except for the data collected over regions with good radar coverage demonstrated in Fig. 14.
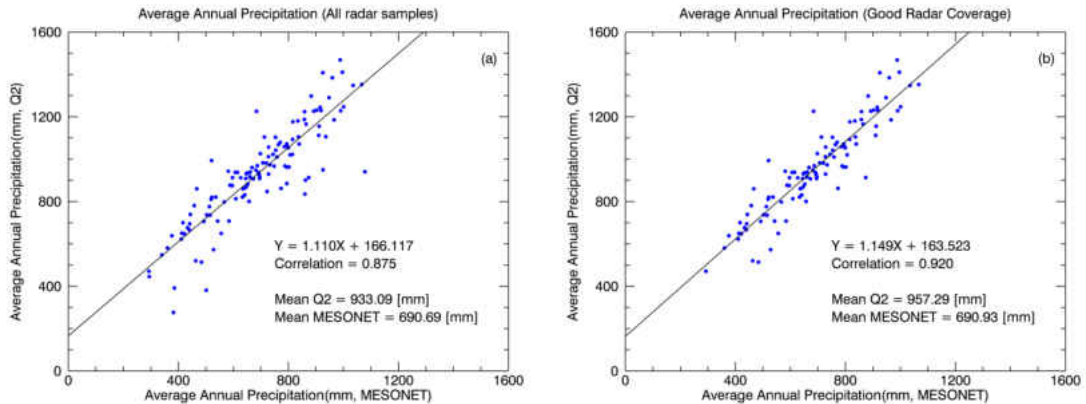
Figure 16. Each blue dot represents the average annual precipitation (2010-2012) observed at a MESONET station and the collocated Q2 estimate for a grid box of 1 km * 1 km containing the MESONET station. (a) All available collocated MESONET and Q2 observations (N1=119), (b) only for the stations (N2=106) after removing data points where MESONET stations were located in the regions of poor radar coverage (bottom of base beam height > 1219 m AGL).

Based on all available radar samples, a linear relationship between Q2 estimates and MESONET observations was found with a strong correlation of 0.875 (Fig. 16a) although Q2 estimates were still much higher than MESONET observations for most cases. After removing the data points where MESONET stations were located in the regions of poor radar coverage, the linear relationship still holds and the correlation increases to 0.92 (Fig. 16b). Limiting the comparison to only regions of good radar coverage increases the slope of the regression line in addition to increasing correlation. Note that the difference between Q2 estimates and MESONET observations in Figs. 12 and 16a are the same ($\sim$ 35%), while the difference is $\sim$38.6% in Fig. 16b. This result indicates that the actual positive bias of

Q2 precipitation estimates may be slightly larger than the value calculated using all qualities of radar coverage.

Examining the Q2 estimated rain distribution yielded results consistent with MESONET observations. As shown in Table 2, Q2 estimates indicated that ~69.4% of rainfall occurred in CC regions, compared to ~70.5% observed by MESONET.

Table 2. Distribution of Observed and estimated rainfall into DCS components. Constructed using data from 16 days with widespread convection over OK during 2012. SCaMPR RH represents SCaMPR with corrections using modeled RH.

Platform	Percentage of Rainfall in CC	Percentage of Rainfall in SR	Percentage of Rainfall in AC	Percentage of Rainfall in Unclassified/Thin Anvil Regions
MESONET	70.48	25.77	2.32	1.43
Q2	69.41	20.41	6.73	3.45
SCaMPR	12.23	29.62	33.83	24.32
SCaMPR RH	14.67	32.37	32.45	20.51

20.4% of Q2 estimated precipitation fell in SR regions, approximately 5.4% less than what was observed by MESONET. Q2 estimates indicated ~10.1% of precipitation in non-raincore regions compared to ~3.8% observed by MESONET.

SCaMPR vs. OK MESONET

A similar study has been performed to evaluate the SCaMPR retrievals using MESONET observations for the year 2012. Figure 17 shows the Cumulative Frequency Distributions (CFDs) of 24-hr accumulated precipitation from SCaMPR and MESONET with a total of 43,852 collocated samples.
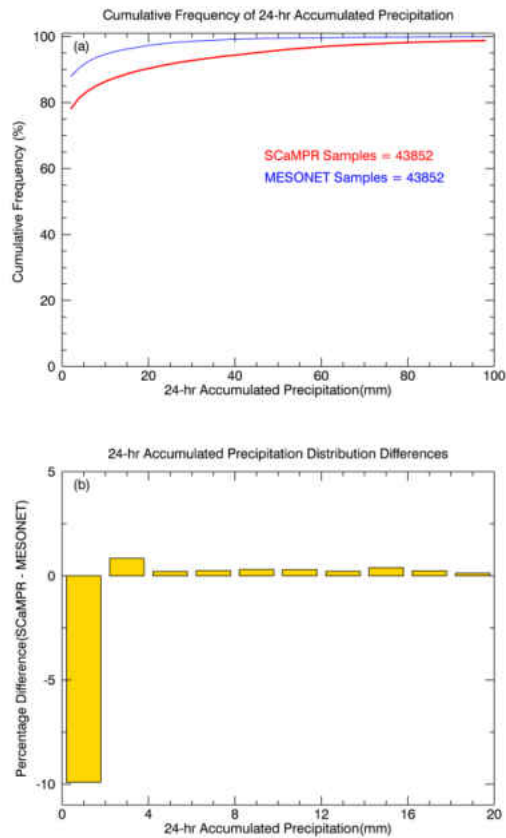
Figure 17. Same as Figure 11, except for the collocated SCaMPR retrievals and MESONET observations for 2012.

The CFD comparison between SCAMPR and MESONET is similar to that between Q2 and MESONET in Fig. 11 except that the SCaMPR CFD starts below 80%. Further study shows that the first bin (0-2 mm) in SCaMPR retrievals is 10% lower than the counterpart of MESONET, indicating that SCaMPR retrievals overestimated precipitation for light rain events. For other bins, the SCaMPR percentages are greater than the corresponding MESONET percentages. These percentage differences are almost an order of magnitude larger than the Q2 vs. MESONET comparison.

A scatterplot for annual precipitation retrieved by SCaMPR and observed by MESONET is presented in Fig. 18 with a modest correlation of 0.567 for a linear relationship.
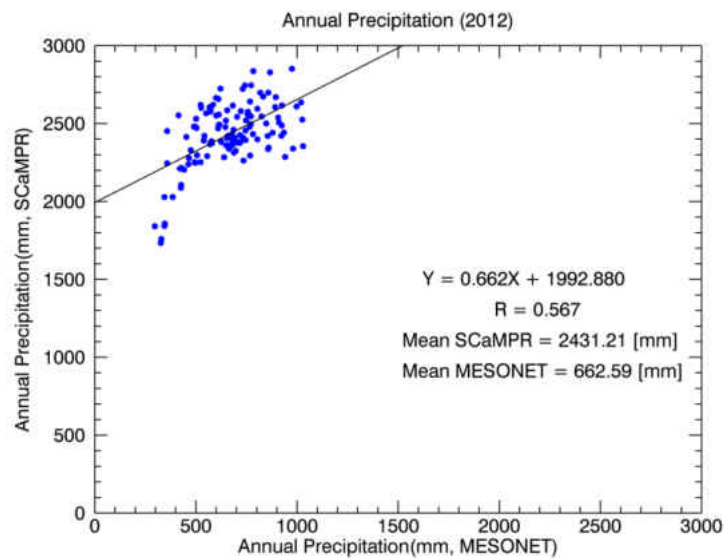
Figure 18. Same as Figure 16, except for the collocated SCaMPR retrievals and MESONET observations for 2012.

However, the SCaMPR retrieved precipitation, on average, is about 3.7 times the MESONET observations with annual precipitation of 2431 mm for SCaMPR and 662.6 mm for MESONET. Nearly 63% of the SCaMPR overestimates across all stations occurred from April through June when precipitation primarily came from intense convection. Statewide 24-hour total precipitation comparisons (not shown) between SCaMPR retrievals and MESONET observations were consistent with their annual

precipitation comparison at each MESONET station. The mean statewide 24-hr total precipitation were 796.8 mm for SCaMPR and 216.9 mm for MESONET, the same ratio as their annual precipitation, but with a stronger correlation of 0.678.

The precipitation distribution from SCaMPR estimates was significantly different from the MESONET observed precipitation distribution as shown in Table 2. A large dry bias occurred in the CC region, where only ~12.2% of SCaMPR estimated precipitation fell compared to the ~70.5% observed by MESONET. However, a significant wet bias occurred in the non-raincore regions where SCaMPR estimated precipitation was 58.2% versus ~3.8% observed by MESONET. For the SR region, the SCaMPR estimated precipitation percentage was 29.6%, only 3.9% greater than the MESONET observed percentage. Inclusion of RH (relative humidity) corrections into the SCaMPR algorithm reduced the amount of precipitation in non raincore regions by ~5.2%.

Comparison of Algorithms

Table 3. Areal coverage of estimated anvil region precipitation for 16 days with widespread convection over OK in 2012.

Platform	Areal Coverage of Anvil Precipitation (km^2)
Q2	1.495×10^6
SCaMPR	1.417×10^7
SCaMPR RH	1.186×10^7
New Algorithm	1.216×10^6

An analysis of 16 days with widespread convection showed that the new algorithm using both optical depth and IR BTs estimated the areal coverage of precipitating anvil regions to be 1.216 x 10^6 km^2 compared to 1.495 x 10^6 km^2 from Q2 estimates (Table 3). As shown in Table 3, both SCaMPR and SCaMPR RH estimates for anvil precipitating area for this time period were roughly an order of magnitude larger than Q2 estimates. Although SCaMPR RH did reduce the size of estimated precipitating anvil area compared to SCaMPR, SCaMPR RH estimates of precipitating anvil area still greatly exceed values observed by ground based radar.

An example of an individual large DCS contributing to this significant difference is shown in Figure 19 where the estimated precipitating area from SCaMPR retrievals is ~26.4 % larger than that from Q2 estimates. The new algorithm in the center of Figure 19 has reduced the SCaMPR overestimate of precipitating area by nearly 22%, and more closely resembles the Q2 estimated precipitating area. The large overestimate or precipitating anvil area size by SCaMPR and the significant improvements made by the new algorithm during a large DCS as shown in Figure 19 represent a common occurrence during this 16 day period of study.

While most of the differences between algorithms occurred during large DCSs, even in smaller DCSs significant differences were present. Figure 20 represents a comparison of the three algorithms as in Figure 19, except for a relatively small DCS. Again, the SCaMPR estimate for precipitating area, ~ 22.4%, is greater than that of the new algorithm, ~8.7%, and Q2, ~9.6%.   The primary source of precipitating anvil area

Figure 19. Q2 Estimated rainfall for the hour ending at 23 UTC 11 May 2011 (a), estimated precipitating area for the hour ending 23 UTC 11 May 2011 from the new algorithm (b), and SCaMPR estimated rainfall for the hour ending at 23 UTC 11 May 2011.

overestimation can be seen in southwestern Oklahoma and northern Texas where SCaMPR estimates show a broad and roughly circular precipitation shield compared to the smaller, and more irregular precipitating areas depicted by the new algorithm and Q2 estimates (Figure 20).
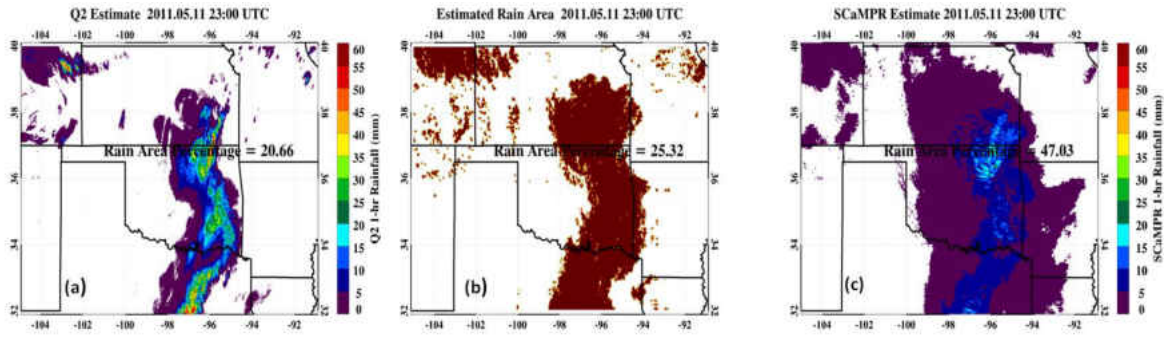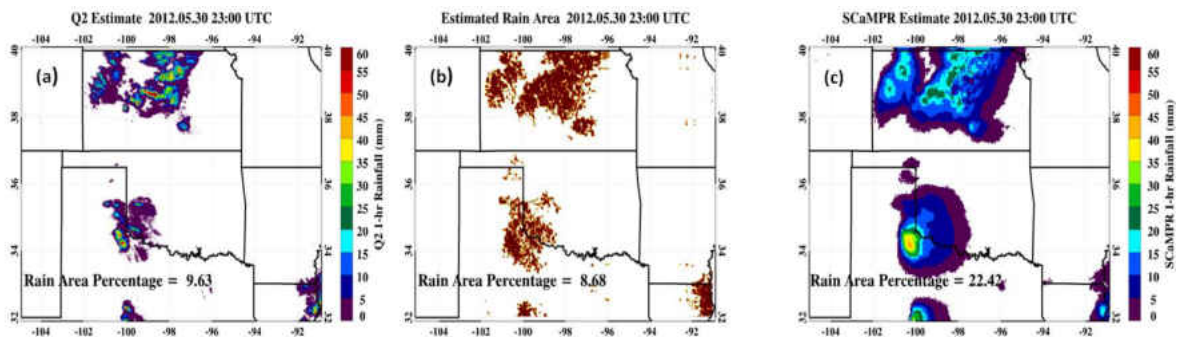

Figure 20. Q2 Estimated rainfall for the hour ending at 23 UTC 30 May 2012 (a), estimated precipitating area for the hour ending 23 UTC 30 May 2012 from the new algorithm (b), and SCaMPR estimated rainfall for the hour ending at 23 UTC 30 May 2012.

CHAPTER IV

DISCUSSION

Despite having a wet bias, Q2 estimates were very strongly correlated with MESONET observations, while SCaMPR estimates suffered from a very large wet bias likely due to excessive precipitation retrievals from anvil regions of DCSs. Q2 estimates were strongly correlated with MESONET observations for 24-hr accumulated precipitation at each MESONET station (0.881), statewide 24-hr total precipitation (0.943) and average annual precipitation (0.92). Q2 estimates were consistently higher (~ 35%) than collocated MESONET observations regardless of timescale (24-hr vs. annual) and spatial coverage (one MESONET station vs. all OK MESONET stations), particularly during the warm season when more intense convection occurred. However, despite these consistent overestimates, the distribution of precipitation into the DCS regions from Q2 estimates closely matched MESONET observations, particularly in the CC regions. Slight differences occurred in the SR and non-raincore regions, where the tipping bucket limitations (0.25 mm) in MESONET observations would create bias favoring SR precipitation over non-raincore precipitation. SCaMPR retrievals were weakly correlated to MESONET observations at the 24-hr timescale and modestly correlated at an annual timescale. Regardless of timescale, SCaMPR estimates drastically overestimated precipitation compared to MESONET observations as noted in Zhang et al. 2013.

Furthermore, the distribution of SCaMPR estimates showed a strong dry bias for raincore regions, and a strong wet bias for anvil regions.

Although it does not seem sampling errors were significant in this study, sampling errors are possible when comparing both the 1-km by 1-km Q2 grid box and 4-km by 4-km SCaMPR grid box estimates to point observations from MESONET. For example, intense precipitation could occur over part of the grid box where the MESONET station is not located, making the gridbox estimate higher than the point observation. While errors such as these are unavoidable for this study and similar studies, with a sufficiently large sample size it is anticipated that occurrences where localized precipitation maxima inside the grid box missed the point observation or passed directly over the point observation will tend to balance one another over time. Part of this impact is likely apparent in the trend of observing stronger correlations between the estimates and observations as the time scale of comparison was increased. While this source of error does not appear to be very significant for this study, it could require special attention for studies utilizing much smaller sample sizes for comparison.

Strengths and Weaknesses of Q2 Estimates

The strong correlations between Q2 estimates and MESONET observations regardless of timescale or spatial coverage make it possible to use Q2 estimates as a substitute for surface rain-gauge networks in the studies where finer spatial and temporal resolution is needed. However, the 35% wet bias in Q2 estimates must be considered, although it is likely an upper bound of the Q2 estimate errors because rain gauges are prone

to underestimate rainfall during intense precipitation events (http://www.mesonet.org/index.php/site/about/moisture_measurements). Furthermore, with simple linear relationships between Q2 estimates and MESONET observations, Q2 estimates could be easily adjusted to better represent ground truth. However, further studies are required to quantitatively determine the Q2 overestimates and the catchment errors associated with tipping bucket rain gauges used in the OK MESONET during different seasons (Humphrey et al. 1997; Nespor and Sevruk 1999; Sevruk 1985; Steiner et al. 1999). Based on this study, bias-adjusted Q2 estimates in the regions such as the Southern Great Plains and Southeast U.S. should be reliable because precipitation is mainly in liquid phase and dominated by convective events where the highest correlations between Q2 estimates and MESONET observations were found.

The primary weakness of Q2 estimates is a discontinuity in precipitation estimates depending on available radar coverage. While Q2 estimates have strong correlations with MESONET observations in the regions of good radar coverage, this is not true in the areas where radar coverage is less sufficient. As the base beam height of the available radar coverage increased, Q2 estimates shift from overestimates to underestimates compared to MEOSNET observations. This change reduces the correlations from 0.92 for good radar coverage to 0.875 for all radar samples as illustrated in Fig. 5. Although the correlation for all radar samples is still strong, caution must be taken because these underestimates may mask the tendency of Q2 to overestimate. As the base beam height increases, the probability that precipitation will be overshot and therefore underestimated by Q2 also

increases. While the magnitude of this difference is not significantly large in most cases,

depending on the specific use of Q2 estimates, this factor should be carefully considered

when using estimates from the regions of poor radar coverage.

Evaluation of SCaMPR

SCaMPR retrievals overestimated precipitation at all MESONET stations for 2012,

with overestimates of annual precipitation ranging from 1400 mm to 2000 mm (Fig. 18).

Correlations between SCaMPR retrievals and MESONET observations were relatively low

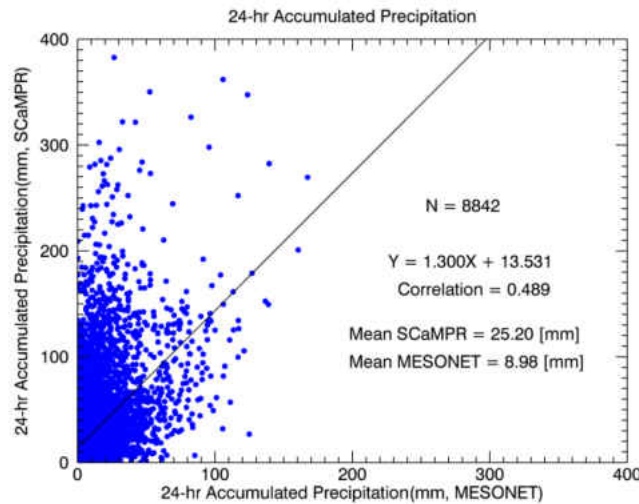on an annual time scale (0.567) and even lower at a 24-hour time scale (Fig. 21).

Figure 21. Same as Figure 10a, except for SCaMPR retrievals and MESONET observations for 2012.

While the direct comparison between the SCaMPR 4km by 4km pixels and point

observations from MESONET stations may reduce the correlations to some degree, the

low correlations arise primarily from SCaMPR precipitation retrievals during the following

situations. Quite often SCaMPR retrieved precipitation from the anvil regions of DCSs, while the collocated MESONET stations recorded nothing. This is apparent in Table 2, where the majority of SCaMPR estimated precipitation occurred in non-raincore regions. These excessive precipitation retrievals from anvil regions are most likely due to the limitation of SCaMPR retrievals arising from SCaMPR's dependence on cloud-top IR brightness temperature. This problem as well as possible cirrus contamination could be responsible for the majority of SCaMPR overestimates during DCS events (Zhang et al. 2013). Therefore, it is necessary to quantitatively estimate the SCaMPR retrievals (and Q2 estimates) under different precipitation ranges using collocated MESONET observations as a ground truth. In an unpublished study, we found that there is a much lower incidence of false alarms than in this study when comparing the full version of the algorithm using SEVIRI data with TRMM data. This suggests that the SCaMPR algorithm will perform significantly better when it is run on the GOES-R Advanced Baseline Imager instead of on the current GOES imager.

Categorical Scores for Q2 and SCaMPR

Categorical scores were calculated for both the 24-hr accumulated Q2 precipitation estimates and SCaMPR retrievals using thresholds of 0.25 mm, 2.5 mm, 12.5 mm, and 25.0 mm from MESONET observations. Probability Of Detection (POD), False Alarm Rate (FAR), and Critical Success Index (CSI) were calculated for each of these thresholds. The Q2 categorical scores were computed for two periods: 2010-2012 and 2012 only, while SCaMPR retrieval categorical scores were calculated only for 2012 to allow a direct

comparison to the Q2 estimates. As shown in Table 4, progressing from the 2.5 mm threshold to the 25.0 mm threshold, both POD and CSI of Q2 estimates decreased while FAR increased.

Table 4. Categorical scores for SCaMPR retrieved precipitation (2012), Q2 estimates (2010-2012), and Q2 Estimates (2012) for 24-hour periods.

Range (mm)	Q2 POD (all)	Q2 FAR (all)	Q2 CSI (all)	SCaMPR POD (2012)	Q2 POD (2012)	SCaMPR FAR (2012)	Q2 FAR (2012)	SCaMPR CSI(2012)	Q2 CSI (2012)
≥0.25	0.78	0.37	0.53	0.75	0.83	0.50	0.37	0.53	0.56
≥2.5	0.85	0.27	0.64	0.81	0.89	0.59	0.24	0.64	0.69
≥12.5	0.84	0.31	0.61	0.83	0.84	0.72	0.31	0.61	0.61
≥25.0	0.81	0.40	0.53	0.78	0.80	0.83	0.42	0.53	0.51

This observed trend is consistent with the Wu et al. (2012) results, but the decreased magnitudes in POD are significantly different. In the Wu et al (2012) study the PODs dropped significantly as the threshold level increased, while the POD decreased only 0.04 from 0.85 to 0.81 in this study. Using 0.25 mm as an additional threshold that was not used in the Wu et al. (2012) study, a relatively high FAR of 0.37 for Q2 estimates was observed. This relatively large FAR is most likely attributed to very light precipitation that evaporated before reaching the ground and occasional ground clutter problems (as demonstrated in Fig. 22 caused by beam ducting from temperature inversions (Turton et al 1988). Figure 22 represents an example when clear skies were present over OK, but Q2 indicated precipitation.
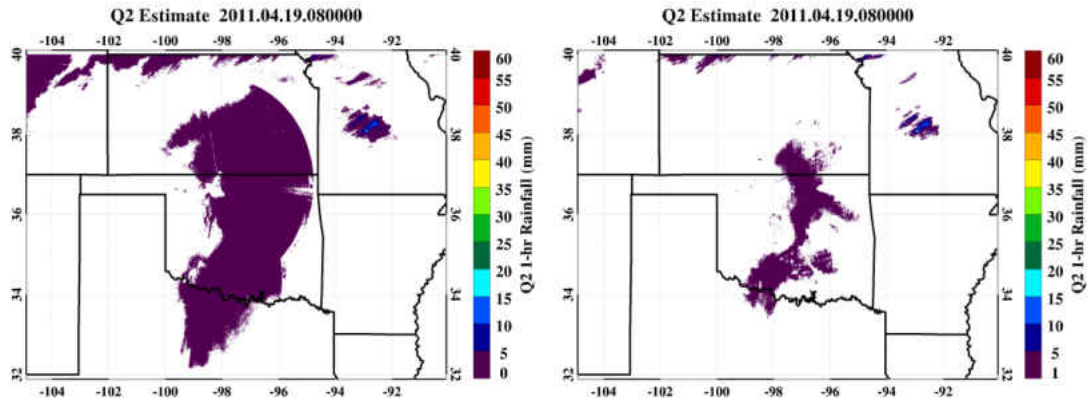
Figure 22. An illustration of the ground clutter contribution to Q2 estimated precipitation with precipitation starting at 0 mm (left) and 1 mm (right). At this time clear skies were reported over OK.

Although the contribution of Q2 overestimates from ground clutter is quite small (Fig. 22), a binary precip/no-precip threshold was used to identify this issue in the FAR and CSI scores.

The categorical scores for SCaMPR retrievals were consistent with expectations based on the large overestimates from precipitation retrievals in non-precipitating regions of DCS's. FAR increased as the threshold level increased, ranging from 0.50 at the 0.25-mm threshold to 0.83 at the 25.0-mm threshold. This increase can be attributed to retrievals of heavy precipitation from non-precipitating and lightly precipitating portions of DCSs, which cause FAR to increase as the frequency of heavy precipitation estimates drop more slowly than actual occurrences of these events. Although SCaMPR POD scores were high and close to Q2 values, FAR scores rose to 0.83 at the 25.0-mm threshold, resulting in much lower CSI scores (0.16). Therefore, it is important to improve the SCaMPR retrieval

algorithms in the future, particularly for the conditions that produce high FAR and low CSI scores.

   An analysis of RMSEs for both Q2 and SCaMPR was consistent with expectations based on the skill scores and linear regression fits. As shown in Table 5, both Q2 and SCaMPR RMSEs rose as the amount of recorded precipitation increased. For the 0.25 mm to 2.5 mm precipitation bin in Table 5, the SCaMPR RMSE (10.26 mm) is nearly 8 times the Q2 RMSE (1.30 mm). This large difference in RMSE between Q2 and SCaMPR can be attributed to SCaMPR precipitation retrievals in non-precipitating regions of DCS's.

Table 5. Root Mean Square Error (RMSE) for 24-hr Q2 and SCaMPR. The ranges used for the calculations are determined from the MESONET observations. Q2 RMSE is shown for all data (2010-2012) and for only 2012 data.

Range (mm)	Q2 RMSE (mm) (all)	Q2 RMSE (mm) (2012)	SCaMPR RMSE (mm) (2012)
$0 \leq x < 2.5$	1.07	1.30	10.26
$2.5 \leq x < 12.5$	7.09	7.20	36.59
$12.5 \leq x < 25$	11.73	12.82	55.44
$25 \leq x$	21.62	24.27	61.03

As illustrated in Fig. 23, SCaMPR retrieved precipitation over northern MO and eastern AR (Fig. 23f) due to cold cloud-top temperature, whereas Q2 estimates (Fig. 23d) and a modified SCaMPR algorithm (Fig. 23e) showed nothing over this region.
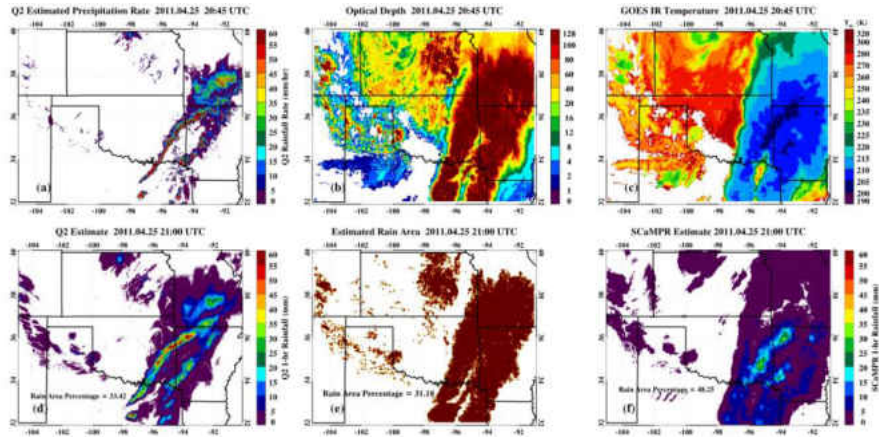
Figure 23. Instantaneous (a) Q2 estimated precipitation rate (mm/hr), (b) GOES-retrieved cloud optical depth, and (c) IR temperature (K) at 20:45 UTC 25 April 2011. Accumulated (d) Q2 estimated rainfall (areal coverage 33.4%), (e) estimated rain area (31.1%) from the newly developed algorithm using both cloud optical depth and IR brightness temperature, and (f) SCaMPR retrieved rainfall (areal coverage 48.3%) over the large domain during 20:00-21:00 UTC 25 April 2011.

Evaluation of New Algorithm

The modified SCaMPR algorithm, employing both cloud optical depth and IR brightness temperature, can significantly reduce the spatial extent of the SCaMPR estimated precipitation, particularly over the anvil regions of DCSs. As illustrated in Figs. 23e and 23f, the SCaMPR precipitation areas were reduced to 31% in the modified version from 48% in its original algorithm (IR temperature only). The new coverage is very close to the Q2 estimated precipitation coverage (33%, Fig. 23d). A more robust comparison covering 14 convective events during the MC3E campaign at the ARM SGP site has also shown the precipitation area estimated from the modified algorithm (9.64%) is closer to the Q2 estimation (12.06%) than that (19.11%) from the SCaMPR original algorithm (Fig.

50

24). These results during the MC3E campaign were consistent with those shown in Table 4 during a 16 day evaluation in 2012.

Additionally, the distribution of precipitation into DCS components was examined for the 16 days with significant convection during 2012. The new rain mask was applied to both SCaMPR and SCaMPR RH, with the results shown in Table 6. The application of the new rain mask to SCaMPR reduced the percentage of total estimated precipitation that fell in anvil areas from ~ 57.1% to ~ 32.4% (Table 6). The majority of SCaMPR estimated rainfall now falls in raincore regions with the rain mask applied. Similar improvements were seen when the rain mask was applied to SCaMPR RH, with the percentage of total precipitation estimated in anvil regions dropping from ~42.2% to ~ 29.7 % (Table 6).
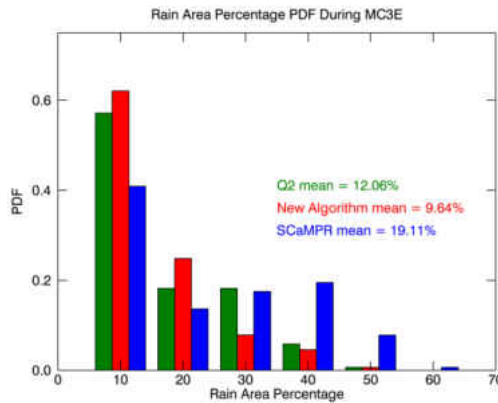
Figure 24. Probability Density Functions (PDF) of rain area percentage using a bin width of 10 % during the Midlatitude Continental Convective Clouds Experiment (MC3E) campaign (14 days with convection) at the ARM SGP site. The 0.25 mm threshold was used for both Q2 and SCaMPR to determine whether or not a pixel was classified as raining.

Table 6. Same as table 2 with SCaMPR Mask and SCaMPR Mask RH added. SCaMPR Mask represents SCaMPR with the new algorithm applied to reduce the estimated precipitating area. SCaMPR Mask RH is the same as SCaMPR Mask, except the new algorithm is applied to SCaMPR RH output.

Platform	Percentage of Rainfall in CC	Percentage of Rainfall in SR	Percentage of Rainfall in AC	Percentage of Rainfall in Unclassified/Thin Anvil Regions
MESONET	71.01	24.55	2.46	1.97
Q2	69.75	24.31	4.46	1.49
SCaMPR	12.23	30.68	35.21	21.88
SCaMPR RH	15.46	40.48	31.15	12.91
SCaMPR Mask	20.78	46.82	29.05	3.36
SCaMPR Mask RH	21.36	48.95	26.93	2.76

The results in Table 6 provide quantitative results for how the application of the new rain mask impacts the characteristics of SCaMPR retrievals. For application to both SCaMPR and SCaMPR RH, the new rain mask is successful in reducing anvil precipitation and creating an overall distribution of precipitation among DCS components that more closely resembles the observed distribution. This new algorithm and its performance will be discussed in much greater detail in future work.

CHAPTER V

CONCLUSIONS

With the immensely better spatial and temporal coverage and resolution compared to rain gauge networks, and the strong correlations with gauge observations, Q2 estimates can serve as a reasonable substitute for ground truth to validate satellite precipitation retrievals in the future as long as the 35% wet bias in Q2 estimates is adequately adjusted or accounted for. Although Q2 estimates were much higher than MESONET observations during the warm season, an excellent agreement was reached for the cold season, and there were strong correlations in both seasons. Additionally, the precipitation distribution among DCS components from Q2 estimated precipitation strongly resembled the MESONET observed distribution. The similarity of the precipitation distributions indicates that although Q2 has a wet bias in this region, it accurately captures the precipitation characteristics of DCSs. Furthermore, with the MESONET stations likely underestimating the true precipitation amounts during DCSs, the wet bias calculated for Q2 during this study is likely an upper bound. While these overestimates could be adjusted using the best fit linear regression equations, further studies are needed to determine the extent of required adjustments. The catchment errors in MESONET observations should be carefully analyzed and considered before adjusting Q2 estimates (Sevruk 1985; Nespor and Sevruk 1999; Humphrey et al. 1997).

Minor ground clutter issues were detected, but the contribution of ground clutter to Q2 precipitation estimates was negligible. It also seemed that virga could possibly be causing Q2 overestimates during light precipitation events, or in cases where no precipitation was observed. Again, this effect was very minor, producing only very small overestimates at times. However, caution should be taken in using Q2 estimates for binary rain/no-rain distinction at a threshold value is 0.25 mm if conditions are conducive to producing ground clutter such as temperature inversions (Turton et al. 1988).

SCaMPR retrievals were much higher than the collocated MESONET observations, by a factor of three to four times. The severe overestimates in SCaMPR retrievals were primarily caused by precipitation retrievals over the anvil regions of DCSs when collocated MESONET stations recorded no precipitation. This problem is most apparent in the precipitation distribution among DCS components where the majority of SCaMPR estimated precipitation falls in anvil regions rather than the raincore regions. These precipitation retrieval problems contributed significantly to the high FAR and lower CSI for SCaMPR retrievals. The bulk of these overestimates mainly occurred from April through June which had frequent intense convective systems. As POD scores are already quite high, reducing the FAR would make SCaMPR a valuable and reliable source of precipitation estimates.

The problem of excessive SCaMPR estimated precipitation rates over the anvil regions of DCSs can be corrected by utilizing NMQ Q2 estimates, and GOES cloud optical depth and IR temperature retrievals. A strong optical depth gradient was found between

the precipitating and non-precipitating (anvil) regions of DCSs although their cloud-top temperatures are nearly the same. This strong gradient can be used to identify the precipitating and non-precipitating regions of a DCS. A new algorithm that utilizes these findings effectively reduced the precipitating area estimated, making significant improvements upon the SCaMPR algorithm. While cloud optical depth does appear to better capture the spatial features of precipitating areas, IR brightness temperature is still superior in providing information about the intensity of precipitation (Fig. 23c).

Similar studies for other regions of the CONUS should be performed to investigate the similarities and differences in precipitation characteristics of DCSs between the SGP and other regions. These studies will provide insights into potential regional similarities and differences in DCSs that can be used for algorithm development and forecasting. With the NWS radar network now having dual polarization capabilities, hail cores could also be added as a DCS component, possibly allowing further understanding of DCSs.

CHAPTER VI

FUTURE WORK

As the new algorithm developed in this study only identifies areas where precipitation is occurring, the next step would be assigning precipitation rates to areas identified as precipitating. To assign rates to pixels determined as precipitating, cloud top BTs and cloud optical depth will be regressed against Q2 estimated precipitation rates. Precipitation rates for the new algorithm will be derived from this regression analysis.

While cloud optical depth and cloud top BTs were focused on in this study, other cloud microphysical properties such as liquid water path will be examined as possible variables to be used in estimating precipitation rates. Furthermore, model data and recent observations of upper level winds, RH, precipitable water, and other relevant meteorological variables will be incorporated into the regression analysis to produce an estimated rain rate. Although the foundation of the new algorithm's estimates will be based on data from the GOES satellites, both model data and observations are available and can be processed with a short enough latency to be included in this proposed operational algorithm.

In addition to the increase of meteorological variables to determine estimated precipitation rates, topographic impacts will also be incorporated. As upslope flows produce enhanced precipitation and downslope flows can produce precipitation shadows,

inclusion of these effects will greatly aid the accuracy of precipitation estimates. Since the topography of the United States is unchanging with respect to the applications of this algorithm, specific pixels can be parameterized for anticipated topographic influences on precipitation that can in some cases dominate over the other variables used in the regression to construct precipitation estimates.

The limitations of the current algorithm to identify precipitating pixels will also be addressed in future studies. While the current limitations of the retrievals of cloud optical depth make the current algorithm reliable only in daylight hours, the newly developed VIIRS day-night band (DNB) images are allowing optical depth to be retrieved reliably at night using reflected moonlight (Figure 25). However, while this improvement is only possible using polar orbiting satellites, its reliance on moonlight will only provide reliable optical depth retrievals less than 50% of nighttime. Furthermore, incorporation of this data from polar orbiters could be problematic in terms of increasing latency of a final precipitation product. Even so, with the additional IR bands on the ABI imager on GOES-R, improved nighttime optical depth retrievals may be possible resembling those shown in Figure 25.

To address the remaining hours during the night, the GOES GLM sensor will be used to include lightning data to aid in determining precipitating area. As lightning occurs in both the CC and SR regions of DCSs, flash rates can be substituted into the
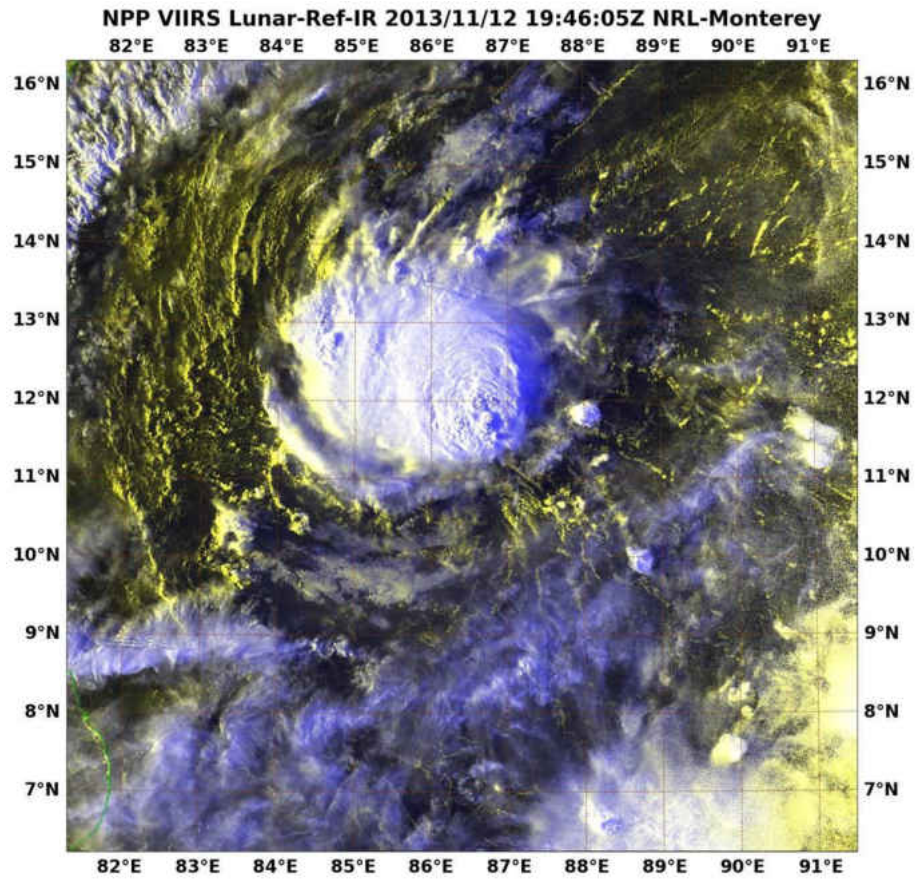
Figure 25. VIIRS DNB image of convection provided by the Naval Research Lab in Monterey, California.

precipitating area algorithm for optical depth retrievals when optical depth retrievals are unavailable. Flash rates can be used as a rain mask similar to how optical depth is used during daylight as lightning is typically most prevalent in precipitating regions of DCSs as shown in Figure 26.
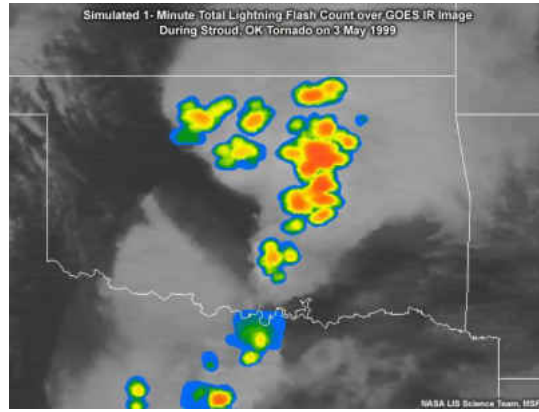
Figure 26. Simulation of contoured flash count possible with the GOES-R GLM
superimposed over a GOES IR image.
Source: http://www.meted.ucar.edu/goes_r/abi

By utilizing improved nighttime optical depth retrievals and GLM lightning data, it
appears the algorithm developed in this study can be made reliable for nearly the entire
day. Time periods around dusk and dawn may continue to be problematic as difficulty
with optical depth retrievals during these times will likely persist, and the performance of
GLM lightning detection is not as strong during daylight hours.

In addition to refinement and completion of the algorithm developed in this study
so that it can become operationally useful, the structure and precipitation characteristics
of DCSs should be evaluated over different regions on the CONUS. Tracking codes can
be used to create an archive of DCSs over the CONUS, allowing the study of these
systems from initiation through dissipation. With dual polarization radar technology now
available throughout the NEXRAD network, hail cores (HC) may be added as a
classification to go with CC, SR, and AC. Lifecycle analysis of DCSs over different
regions may provide information to further improve precipitation estimates, while also

providing information potentially useful to forecasters. Lastly, future studies are needed

comparing the performance of Q2/Q3 estimates to dual polarization rainfall estimates.

REFERENCES CITED

Adler, F. R., and A. J. Negri, 1988: A satellite infrared technique to estimate tropical convective and stratiform rainfall. *J. Appl. Meteor.*, **27**, 30–51.

Amitai, E., W. Petersen, X. Llort, and S. Vasiloff, 2012: Multiplatform comparisons of rain intensity for extreme precipitation events. *IEEE Trans. Geosci. Remote Sens.*, **50**, 675-686.

Andrieu, H., J. D. Creutin, G. Delrieu, and D. Faure, 1997: Use of a weather radar for the hydrology of a mountainous area. Part I: Radar measurements interpretation. *J. Hydrol.*, **125**, 1–25.

Austin, P. M., 1987: Relation between measured radar reflectivity and surface rainfall. *Mon. Wea. Rev.*, **115**, 1053–1070.

Chen, Sheng, and Coauthors, 2013: Evaluation and Uncertainty Estimation of NOAA/NSSL Next-Generation National Mosaic Quantitative Precipitation Estimation Product (Q2) over the Continental United States. *J. Hydrometeor*, **14**, 1308–1322.

Ebert, E. E., J. E. Janowiak, and C. Kidd, 2007: Comparison of near-real-time precipitation estimates from satellite observations and numerical models. *Bull. Amer. Meteor. Soc.*, **88**, 47–64.

Feng, Z., X. Dong, and B. Xi, 2009: A method to merge WSR-88D data with ARM SGP millimeter cloud radar data by studying deep convective systems. *J. Atmos. Ocean. Techn.* **26**, 958-971.

-----, -----, -----, C. Schumacher, P. Minnis, and M. Khaiyer, 2011: Top-of-atmosphere radiation budget of convective core/stratiform rain and anvil clouds from deep convective systems, *J. Geophys. Res.*, **116**, D23202, doi:10.1029/2011JD016451.

-----, -----, -----, S. McFarlane, A. Kennedy, B. Lin, and P. Minnis, 2012: Life cycle of deep convective systems in a Lagrangian Framework. *J. Geophys. Res.*, **117**, D23201, doi:10.1029/2012JD018362.

Hong, Y., R. F. Adler, A. Negri, and G. J. Huffman, 2007: Flood and landslide applications of near real-time satellite rainfall products. *Nat. Hazards*, **43**, 285–294.

Huffman, G. J., and coauthors, 2007: The TRMM Multisatellite Precipitation Analysis (TMPA): Quasi-global, multiyear, combined-sensor precipitation estimates at fine scales. *J. Hydrometeor.*, **8**, 38-55.

Humphrey, M. D., J. D. Istok, J. Y. Lee, J. A. Hevesi, and A. L. Flint, 1997: A new method for automated dynamic calibration of tipping-bucket rain gauges. *J. Atmos. Ocean. Tech.*, **14**, 1513–1519.

Islam, T., Rico-Ramirez, M.A., 2013: An overview of the remote sensing of precipitation with polarimetric radar, *Progress in Physical Geography*.

Joyce, R. J., J. E. Janowiak, P. A. Arkin, and P. Xie, 2004: CMORPH: A method that produces global precipitation estimates from passive microwave and infrared data at high spatial and temporal resolution.. *J. Hydrometeor.*, **5**, 487-503.

Kirstetter, Pierre-Emmanuel, and Coauthors, 2012: Toward a Framework for Systematic Error Modeling of Spaceborne Precipitation Radar with NOAA/NSSL Ground Radar–Based National Mosaic QPE. *J. Hydrometeor*, **13**, 1285–1300.

Kondragunta, C. R., D. Kitzmiller, D. J. Seo, and K. Shrestha, 2005: Objective integration of satellite, rain gauge, and radar precipitation estimates in the multisensor precipitation estimator algorithm. Preprints, *19th Conf. on Hydrology*, San Diego, CA, Amer. Meteor. Soc., P2.8. [Available online at https://ams.confex.com/ams/Annual2005/techprogram/paper_86219.htm.]

Krajewski, W., and J. Smith, 2002: Radar hydrology: Rainfall estimation. *Adv. Water Resour.*, **25**, 1387–1394.

T. Kubota, S. Shige, H. Hashizume, K. Aonashi, N. Takahashi, S. Seto, M. Hirose, Y. N. Takayabu, K. Nakagawa, K. Iwanami, T. Ushio, M. Kachi, and K. Okamoto, 2007: Global Precipitation Map using Satelliteborne Microwave Radiometers by the GSMaP Project : Production and Validation, *IEEE Trans. Geosci. Remote Sens.*, **45 (7)**, 2259-2275.

Kuligowski, R. J., 2010: *GOES-R Advanced Baseline Imager (ABI) Algorithm Theoretical Basis Document for Rainfall Rate / QPE*. DOC / NOAA / NESDIS, 44 pp. [Available online at http://www.goes-r.gov/products/ATBDs/baseline/Hydro_RRQPE_v2.0_no_color.pdf].

Langston, C., J. Zhang, and K. Howard, 2007: Four-dimensional dynamic radar mosaic. *J. Atmos. Ocean. Tech.*, **24**, 776–790.

Maddox, R., J. Zhang, J. Gourley, and K. Howard, 2002: Weather radar coverage over the contiguous United States. *Wea. Forecasting*, **17**, 927–934.

Minnis et al. (2011) CERES Edition-2 cloud property retrievals using TRMM VIRS and Terra and Aqua MODIS data, Part II: Examples of average results and comparisons with other data. IEEE Trans. Geosci. Remote Sens. 49,4401-4430.

Negri, A. J., and R. F. Adler, 1981: Relationship of satellite-based thunderstorm intensity to radar-estimated rainfall. *J. Appl. Meteor*., **20**, 288–300.

Nešpor, V., and B. Sevruk, 1999: Estimation of wind-induced error of rainfall gauge measurements using a numerical simulation. *J. Atmos. Ocean. Tech*., **16**, 450–464.

Park, Hyang Suk, A. V. Ryzhkov, D. S. Zrnić, Kyung-Eak Kim, 2009: The Hydrometeor Classification Algorithm for the Polarimetric WSR-88D: Description and Application to an MCS. *Wea. Forecasting*, **24**, 730–748.

Scofield, R. A., and R. J. Kuligowski, 2003: Status and outlook of operational satellite precipitation algorithms for extreme-precipitation events. *Wea. Forecasting*, **18**, 1037–1051.

Sevruk, B., 1985: Correction of precipitation measurements. Proc. *Workshop on the Correction of Precipitation Measurements*, Zurich, Switzerland, WMO/IAHS/ETH, 13–23.

Smith, J. A., D. J. Seo, M. L. Baeck, and M. D. Hudlow, 1996: An intercomparison study of NEXRAD precipitation estimates. *Water Resour. Res.*, **32**, 2035–2045.

Sorooshian, S., K. Hsu, X. Gao, H.V. Gupta, B. Imam, and D. Braithwaite, 2000: Evaluation of PERSIANN system satellite-based estimates of tropical rainfall, *Bull. Amer. Meteor. Soc.*, **81**, 2035-2046.

Steiner, Matthias, Robert A. Houze, Sandra E. Yuter, 1995: Climatological Characterization of Three-Dimensional Storm Structure from Operational Radar and Rain Gauge Data. *J. Appl. Meteor*., **34**, 1978–2007.

Steiner, M., J. A. Smith, S. J. Burges, C. V. Alonso, and R. W. Darden, 1999: Effect of bias adjustment and rain gauge data quality control on radar rainfall estimation. *Water Resour. Res*., **35**, 2487–2503.

Turk, F. J., E. E. Ebert, H.-J. Oh, B.-J. Sohn, V. Levizzani, E. A. Smith, and R. Ferraro, 2013: Validation of an operational global precipitation analysis at short time scales. Preprints, *12th Conf. Sat. Met. Ocean.*, 2003. Amer. Meteor. Soc., CD-ROM, J1.2.

Turton J. D., D. A. Bennetts and S.F.G. Farmer, 1988: An introduction to radio ducting, *Meteor. Mag.*, **117**, 245-254.

Vicente, G. A., R. A. Scofield, and W. P. Menzel, 1998: The operational GOES infrared rainfall estimation technique. *Bull. Amer. Meteor. Soc.*, **79**, 1883–1898.

Villarini, G., and W. Krajewski, 2010: Review of the different sources of uncertainty in single polarization radar-based estimates of rainfall. *Surv. Geophys.*, **31**, 107–129.

Wilson, James W., Edward A. Brandes, 1979: Radar measurement of rainfall—A summary. *Bull. Amer. Meteor. Soc.*, **60**, 1048–1058.

Wu, D., X. Dong, B. Xi, Z. Feng, A. Kennedy, G. Mullendore, M. Gilmore, and W-K Tao, 2013: The impact of various WRF single-moment microphysics parameterizations on squall line precipitation. *J. Geophys. Res.*, **118**, 19, DOI: 10.1002/jgrd.50798.

Wu, W., D. Kitzmiller, and S. Wu, 2012: Evaluation of radar precipitation estimates from the National Mosaic and Multisensor Quantitative Precipitation Estimation System and the WSR-88D Precipitation Processing System over the conterminous United States. *J. Hydrometeor.*, **13**, 1080–1093.

Zhang, J., K. Howard, and J. J. Gourley, 2005: Constructing three- dimensional multiple radar reflectivity mosaics: Examples of convective storms and stratiform rain echoes. *J. Atmos. Ocean. Tech.*, **22**, 30–42.

Zhang, J., and Y. Qi, 2010: A real-time algorithm for the correction of brightband effects in radar-derived precipitation estimation. *J. Hydrometeor.*, **11**, 1157–1171.

Zhang, J., et al. (2011), National Mosaic and Multi-Sensor OPEN MQ) System: Description, results, and future plans. *Bull. Amer. Meteor. Soc.*, **92**, 1321-1338.

Zhang, Y., D.-J. Seo, D. Kitzmiller, H. Lee, R. J. Kuligowski, D. Kim, and C. R. Kondragunta, 2013: Comparative strengths of SCaMPR satellite QPEs with and without TRMM ingest versus gridded gauge-only analyses. *J. Hydrometeor*, **14**, 153–170.

Zrnić, Dusan S., Valery M. Melnikov, Alexander V. Ryzhkov, 2006: Correlation Coefficients between Horizontally and Vertically Polarized Returns from Ground Clutter. *J. Atmos. Oceanic Tech.*, **23**, 381–394.